PHYSICAL REVIEW E **105**, 034803 (2022)

Thermal transport mechanism at a solid-liquid interface based on the heat flux detected at a subatomic spatial resolution

Kunio Fujiwara[1,2,*] and Masahiko Shibahara[3]
[1]*Center for Atomic and Molecular Technologies, Osaka University, Suita, Osaka 565-0871, Japan*
[2]*Japan Science and Technology Agency, PRESTO, Kawaguchi, Saitama 332-0012, Japan*
[3]*Department of Mechanical Engineering, Osaka University, Suita, Osaka 565-0871, Japan*

(Received 11 August 2021; accepted 6 February 2022; published 24 March 2022)

Heat flux is a fundamental quantity in thermal science and engineering and is essential for understanding thermal transport phenomena. In this study, the heat flux in a solid-liquid interfacial region is obtained in a three-dimensional (3D) space at a subatomic spatial resolution based on classical molecular dynamics, yielding a 3D structure of the heat flux between the solid and liquid layers in contact. The results using the Lennard-Jones potential reveal the directional qualities of the heat flux, which are significantly dependent on the subatomic stresses in the structures of condensed phase systems. The heat flux and stress at the subatomic scale are related to the macroscopic transport quantities, which can be obtained using distribution functions; the stress and energy flux properties at the subatomic scale are comprehensively investigated using a single-interaction-based stress and energy flux to determine the origin of the thermal transport mechanism at the solid-liquid interface. The findings reveal that the density of states due to the stress caused by a single interaction exhibits a bandlike behavior. The net energy transport comprises positive and negative energy transport inside and outside the band. In addition, this is related to the intrinsic transport property of the atoms and molecules at the solid-liquid interface at the subatomic scale. The difference between the energy transport rates when a solid atom in the vicinity of the interface is near to or far from the liquid phase is the origin of the energy transport mechanism at the solid-liquid interface. 3D analysis of the heat flux and stress is carried out by varying the interaction strengths between the liquid molecules and solid atoms at the solid-liquid interface. This reveals that the directional quality of transport quantities is high at strong interaction strengths, thus indicating enhanced thermal transport. Furthermore, the influence of the temperature gradient in the system suggests that the energy transport imbalance between inside and outside the stress band in a high-stress field at the subatomic scale induces the net thermal transport across the interface in the nonequilibrium state.

DOI: 10.1103/PhysRevE.105.034803

I. INTRODUCTION

The conservation laws of mass, momentum, and energy are fundamental physical principles. Moreover, the derived transport equations (i.e., the continuity, momentum, and energy equations) with the constitutive equations provide a general and effective approach to quantitatively predict transport phenomena based on macroscopic physical properties, such as viscosity, thermal conductivity, and heat capacity. With respect to conservation laws, the mass, momentum, and energy in a volume element are balanced by the sum of the input and output fluxes through the boundary of the volume element where time-varying external forces do not act [1]. Macroscopic quantities, such as the density, pressure, and temperature in a unit volume, allow for an intuitive understanding of macroscopic transport phenomena. Moreover, microscopic expressions corresponding to the macroscopic transport equations were derived and have been used extensively in recent numerical analyses to explore transport phenomena at the nanoscale, or to relate macroscopic transport phenomena to atomic and molecular properties [2,3]. The physical quantities obtained from the microscopic expression are consistent with the macroscopic quantities for a homogeneous system considering a sufficient average over time and space. However, for an inhomogeneous system, the quantities are different from the macroscopic quantities (e.g., interfacial pressure components tangential to the interface) [4,5]. The field quantities of the mass, stress, and energy flux in the microscopic expression reflect the atomic and molecular influences and can be used to examine microscopic transport phenomena at an atomic and molecular scale. However, for significantly smaller spatial and temporal scales, e.g., less than the order of Å and femtoseconds, respectively, where macroscopic thermodynamic quantities cannot be accurately defined, a physically significant interpretation of field quantities in terms of the stress tensor and energy flux becomes extremely difficult. A more straightforward method to determine the underlying physics behind the observed field quantities is therefore required.

Thermal transport across a solid-liquid interface is an important phenomenon in the fields of nanoscience and

---

[*] k.fujiwara@mech.eng.osaka-u.ac.jp

nanotechnology. Moreover, thermal transport across solid-liquid interfaces has attracted significant research attention, because such transport is critical for several applications, including functional surfaces [6,7], nanofluids [8,9], and nanofluidic devices [10]. To fundamentally understand thermal transport through a solid-liquid interface, the transport properties of atoms and molecules are essential. Therefore, the microscopic theory of such atomic and molecular transport is necessary to better understand this phenomenon. In previous studies on thermal transport across solid-liquid interfaces, the interfacial thermal conductance (ITC) was evaluated using theoretical [11], numerical [12–21], and experimental [22] methods. In these studies, the classical molecular dynamics (CMD) approach has been used to understand the thermal transport properties at an atomic or molecular scale, and CMD is becoming a standard tool used to evaluate the ITC. To elucidate the thermal transport mechanism, the kinetic and configurational components in the microscopic transport equations were evaluated to elucidate their contributions to the thermal conductivity or the net heat flux based on nonequilibrium simulations [23]. Another method involves the calculation of the longitudinal and transverse modes of the heat flux across the interface [24], which is important for phonon-based interpretation using the vibrations of atoms and molecules at the interface region. Thus, the microscopic transport equations have contributed to understanding of the heat flux from atomic and molecular perspectives.

In recent studies [25,26] based on CMD simulations, two-dimensional (2D) heat flux maps were obtained at a subatomic spatial resolution. This revealed that the heat flux across a solid-liquid interface is not uniform along a macroscopic temperature gradient at the single-atom scale. Such local physical quantities detected at an extremely small spatial resolution (subatomic scale: less than 1 Å) allow for the visualization of the heat flow at the nanometer scale and provide critical information to better understand the transport phenomena in such a system. However, quantitative evaluations of the true heat flux (not averaged in space) have not been made, and detecting heat flux in three dimensions remains an issue. Three-dimensional (3D) detection of the heat flux is necessary for a general interpretation of the heat flux as a field transport quantity, which is related to the fundamental energy transfer mechanism at the subatomic scale. Moreover, the relationship between the field transport quantities at the macroscopic and subatomic scale has not been previously determined using the basic Lennard-Jones potential (LJ) model. This is important for the advancement of nanoscience based on an extension of the conservation laws in a specific volume element that is generally used to model the macroscopic dynamics of fluids.

In this study, we investigate the properties of the stress and heat flux at the subatomic scale to determine the mechanism of thermal transport through a solid-liquid interface in the framework of classical molecular dynamics. A numerical technique based on microscopic transport equations is developed to obtain local physical quantities, which is employed to determine the 3D stress and heat flux at the subatomic scale in a solid-liquid interfacial region for a system modeled using the LJ potential. The relationship between the stress and heat flux at the subatomic scale is investigated based on the 3D stress and heat flux structures. Further, a method based on distribution functions is proposed to relate the local physical quantities at the subatomic scale to the physical quantities influenced by a single interaction between particles. Using the method, the properties of the stress and heat flux at the subatomic scale are examined and related to those of the macroscopic stress and heat flux at the solid-liquid interface. Furthermore, the influence of the solid-liquid interaction strength and temperature gradient in the system on the interfacial thermal transport is examined using the single-interaction-based stress and energy flux, and the result provides an explanation of the origin of the thermal transport mechanism at the solid-liquid interface. The remainder of this paper is organized as follows.

In Sec. II, the microscopic expression of the conservation law is considered, and a distribution function considering the influence of the movement of a single particle and single interaction between particles is introduced and related to the local field quantities.

In Sec. III, the numerical details of the simulation are presented. The required calculation time is discussed to understand whether a significant heat flux can be generated at the subatomic scale using classical molecular dynamics.

In Sec. IV, a 2D transport field at a solid-liquid interface is presented, and its difference in comparison with a one-dimensional (1D) transport is discussed.

In Sec. V, a 3D transport field at a solid-liquid interface is presented for various wetting conditions between solid and liquid layers in contact, thus revealing the differences in the stress and heat flux between the macro- and subatomic scales. The results are compared quantitatively with the 1D and 2D results, and the relationship between the stress and heat flux at the subatomic scale is presented.

In Sec. VI, the properties of the density distribution, which depend on the single-interaction-based stress and energy flux, are examined in detail, and the field quantities of the stress and heat flux at macroscopic and subatomic scales are related through the single-interaction-based stress and energy flux.

In Sec. VII, the mechanism of thermal transport across a solid-liquid interface is detailed based on the relationship between the single-interaction-based stress or energy flux and the behavior of the related particle. The thermal transport mechanism at the macroscopic and subatomic scales is presented.

In Sec. VIII, an investigation of the thermal transport mechanism from the single-interaction-based energy flux is presented with respect to various temperature gradients in the system.

In Sec. IX, the conclusions are presented.

In Appendix A, a discussion is presented about the influences of the calculation conditions (i.e., cutoff distance and simulation model size).

In Appendix B, an investigation of thermal transport based on the single-interaction-based energy flux using the velocity of a solid atom and the force acting on the solid atom is presented, and the result is compared with that presented in the main body of the paper, where the velocities of the solid atom and liquid molecule are considered for the heat flux calculation.

II. LOCAL AND INSTANTANEOUS TRANSPORT BASED ON MICROSCOPIC TRANSPORT EQUATIONS AND RELATIONSHIP WITH DENSITY OF STATES DISTRIBUTION BASED ON SINGLE INTERACTIONS AND SINGLE-PARTICLE MOVEMENT

The derivation of the local and instantaneous physical quantities is common knowledge [2,3,27–29]. First, we reconsider the essential points from a phenomenological point of view. We then introduce the density-of-states distribution based on the variables related to the single-particle movement and single interaction between particles. The microscopic field quantities are related to the density-of-states distribution. We start with the general formulation, which is applicable to not only interfaces but also bulk phases.

The mass, momentum, and energy densities at position $\mathbf{r}$ and time t are expressed microscopically using the Dirac δ function for a system that contains N_ξ particles for the species ξ, as follows:

$$\rho(\mathbf{r},t) = \sum_\xi \sum_{i=1}^{N_\xi} m_{\xi,i}\delta(\mathbf{r}-\mathbf{r}_i), \tag{1}$$

$$\rho\mathbf{v}(\mathbf{r},t) = \sum_\xi \sum_{i=1}^{N_\xi} m_{\xi,i}\mathbf{v}_{\xi,i}\delta(\mathbf{r}-\mathbf{r}_i), \tag{2}$$

$$\rho e(\mathbf{r},t) = \sum_\xi \sum_{i=1}^{N_\xi} e_{\xi,i}\delta(\mathbf{r}-\mathbf{r}_i), \tag{3}$$

where m is the mass of the particle, ρ is the density, $\mathbf{v}$ is the velocity vector, and e is the total energy of the particle, which is defined as follows: $e_{\xi,i} = (1/2)m_{\xi,i}\mathbf{v}_{\xi,i}^2 + (1/2)\Sigma_\zeta\Sigma_j\phi_{\xi i,\zeta j}$. In particular, $\phi_{\xi i,\zeta j}$ is the potential energy between the ith particle of species ξ and jth particle of species ζ. By substituting Eqs. (1)–(3) into the balance equations where no external force is considered,

$$\frac{\partial\rho}{\partial t} = -\nabla\cdot(\rho\mathbf{v}), \tag{4}$$

$$\frac{\partial(\rho\mathbf{v})}{\partial t} = -\nabla\cdot(\mathbf{P}+\rho\mathbf{v}\mathbf{v}), \tag{5}$$

$$\frac{\partial(\rho e)}{\partial t} = -\nabla\cdot(\mathbf{J}+\rho e\mathbf{v}+\mathbf{P}\cdot\mathbf{v}), \tag{6}$$

we obtain the microscopic expression of the mass flux $\mathbf{M}$, pressure tensor $\mathbf{P}$, and heat flux $\mathbf{J}$ for the ξ-component system using the pair-potential function [29,30]:

$$\mathbf{M}(\mathbf{r},t) = \sum_\xi \sum_i^{N_\xi} m_{\xi,i}[\mathbf{v}_{\xi,i}-\mathbf{v}(\mathbf{r}_{\xi,i},t)]\delta(\mathbf{r}-\mathbf{r}_{\xi,i}), \tag{7}$$

$$\begin{aligned}\mathbf{P}(\mathbf{r},t) = {} & \sum_\xi \sum_i^{N_\xi} m_{\xi,i}[\mathbf{v}_{\xi,i}-\mathbf{v}(\mathbf{r}_{\xi,i},t)][\mathbf{v}_{\xi,i}-\mathbf{v}(\mathbf{r}_{\xi,i},t)]\delta(\mathbf{r}-\mathbf{r}_{\xi,i}) \\ & -\frac{1}{2}\sum_\xi\sum_\zeta\sum_i^{N_\xi}\sum_{j\neq i}^{N_\zeta}\mathbf{r}_{\xi i,\zeta j}\mathbf{F}_{\xi i,\zeta j}\int_0^1\delta(\mathbf{r}-\mathbf{r}_{\xi,i}-s\mathbf{r}_{\xi i,\zeta j})\,ds,\end{aligned} \tag{8}$$

$$\mathbf{J}(\mathbf{r},t) = \sum_\xi\sum_i^{N_\xi} u_{\xi,i}[\mathbf{v}_{\xi,i}-\mathbf{v}(\mathbf{r}_{\xi,i},t)]\delta(\mathbf{r}-\mathbf{r}_{\xi,i}) - \frac{1}{2}\sum_\xi\sum_\zeta\sum_i^{N_\xi}\sum_{j\neq i}^{N_\zeta}\mathbf{r}_{\xi i,\zeta j}\mathbf{F}_{\xi i,\zeta j}\cdot[\mathbf{v}_{\xi,i}-\mathbf{v}(\mathbf{r},t)]\int_0^1\delta(\mathbf{r}-\mathbf{r}_{\xi,i}-s\mathbf{r}_{\xi i,\zeta j})\,ds, \tag{9}$$

with $\mathbf{r}_{\xi i,\zeta j} = \mathbf{r}_{\zeta,j}-\mathbf{r}_{\xi,i}$ and $u_{\xi,i} = (1/2)m_{\xi,i}[\mathbf{v}_{\xi,i}-\mathbf{v}(\mathbf{r}_{\xi,i})]^2 + (1/2)\Sigma_\zeta\Sigma_j\phi_{\xi i,\zeta j}$. The averaged velocities at $\mathbf{r}$ and $\mathbf{r}_{\xi,i}$ are defined as $\mathbf{v}(\mathbf{r},t)$ and $\mathbf{v}(\mathbf{r}_{\xi,i},t)$, respectively. The integrations of Eqs. (8) and (9) determine whether the point $\mathbf{r}$ is on the line segment between the ith particle of species ξ and jth particle of species ζ, using the variable s $(0\leqslant s\leqslant 1)$.

We consider a system with particles that consists of the local volume Ω at the local point $\mathbf{r}$ (x,y,z) within the finite area $A_\alpha(\mathbf{r})$ $(\alpha = x, y, \text{or } z)$, as shown in Fig. 1, where $A_z(\mathbf{r})$ is the plane normal to the z axis, and is situated at the middle of the local volume Ω. Integrating Eqs. (7)–(9) over the area $A_\alpha(\mathbf{r})$ at the point $\mathbf{r}$ provides the mass flux M_α, pressure tensor $P_{\alpha\beta}$, and heat flux J_α, as follows:

$$M_\alpha(\mathbf{r},t) = \frac{1}{A_\alpha}\sum_\xi\sum_i^{N_\xi} m_{\xi,i}[v_{\xi,i,\alpha}-v_\alpha(\mathbf{r}_{\xi,i},t)]\delta(\alpha_{\xi,i}-\alpha)\Pi\left(\frac{\beta_{\xi,i}-\beta}{\Delta\beta}\right)\Pi\left(\frac{\gamma_{\xi,i}-\gamma}{\Delta\gamma}\right), \tag{10}$$

$$\begin{aligned}P_{\alpha\beta}(\mathbf{r},t) = {} & \frac{1}{A_\alpha}\sum_\xi\sum_i^{N_\xi} m_{\xi,i}[v_{\xi,i,\alpha}-v_\alpha(\mathbf{r}_{\xi,i},t)][v_{\xi,i,\beta}-v_\beta(\mathbf{r}_{\xi,i},t)]\delta(\alpha_{\xi,i}-\alpha)\Pi\left(\frac{\beta_{\xi,i}-\beta}{\Delta\beta}\right)\Pi\left(\frac{\gamma_{\xi,i}-\gamma}{\Delta\gamma}\right) \\ & -\frac{1}{4A_\alpha}\sum_\xi\sum_\zeta\sum_i^{N_\xi}\sum_{j\neq i}^{N_\zeta} F_{\xi i,\zeta j,\beta}[\mathrm{sgn}(\alpha-\alpha_{\xi,i})-\mathrm{sgn}(\alpha-\alpha_{\zeta,j})]\Pi\left(\frac{\beta_\alpha-\beta}{\Delta\beta}\right)\Pi\left(\frac{\gamma_\alpha-\gamma}{\Delta\gamma}\right),\end{aligned} \tag{11}$$

$$J_\alpha(\mathbf{r},t) = \frac{1}{A_\alpha}\sum_\xi \sum_i^{N_\xi} e_{\xi,i}[v_{\xi,i,\alpha} - \bar{v}_\alpha(\mathbf{r}_{\xi,i},t)]\delta(\alpha_{\xi,i}-\alpha)\Pi\left(\frac{\beta_{\xi,i}-\beta}{\Delta\beta}\right)\Pi\left(\frac{\gamma_{\xi,i}-\gamma}{\Delta\gamma}\right)$$

$$- \frac{1}{4A_\alpha}\sum_\xi\sum_\zeta\sum_i^{N_\xi}\sum_{j\neq i}^{N_\zeta}\mathbf{F}_{\xi i,\zeta j}\cdot[\mathbf{v}_{\xi,i} - \bar{\mathbf{v}}(\mathbf{r},t)][\mathrm{sgn}(\alpha-\alpha_{\xi,i}) - \mathrm{sgn}(\alpha-\alpha_{\zeta,j})]\Pi\left(\frac{\beta_\alpha-\beta}{\Delta\beta}\right)\Pi\left(\frac{\gamma_\alpha-\gamma}{\Delta\gamma}\right), \tag{12}$$

where α, β, and γ ($\alpha \neq \beta \neq \gamma$) denote the x, y, or z component, respectively; $\bar{v}(\mathbf{r},t)$ is the averaged velocity at $\mathbf{r}$ with an area of A_α. In Eqs. (10)–(12), sgn and Π are the sign function and rectangle function, respectively, and the definition of the 1D (x') rectangle function: $\Pi[(x'-x)/\Delta x] = \{H[x'-(x-\Delta x/2)] - H[x'-(x+\Delta x/2)]\}$ is used with the Heaviside step function H. In the rectangle functions of Eqs. (11) and (12), β_α is defined as the β coordinate of the point where the line segment of particles i and j intersects the plane at α. The diagonal component $\alpha\alpha$ of the pressure tensor can then be expressed as the same form:

$$P_{\alpha\alpha}(\mathbf{r},t) = \frac{1}{A_\alpha}\sum_\xi\sum_i^{N_\xi} m_{\xi,i}[v_{\xi,i,\alpha} - v_\alpha(\mathbf{r}_{\xi,i},t)][v_{\xi,i,\alpha} - v_\alpha(\mathbf{r}_{\xi,i},t)]\delta(\alpha_{\xi,i}-\alpha)\Pi\left(\frac{\beta_{\xi,i}-\beta}{\Delta\beta}\right)\Pi\left(\frac{\gamma_{\xi,i}-\gamma}{\Delta\gamma}\right)$$

$$- \frac{1}{4A_\alpha}\sum_\xi\sum_\zeta\sum_i^{N_\xi}\sum_{j\neq i}^{N_\zeta} F_{\xi i,\zeta j,\alpha}[\mathrm{sgn}(\alpha-\alpha_{\xi,i}) - \mathrm{sgn}(\alpha-\alpha_{\zeta,j})]\Pi\left(\frac{\beta_\alpha-\beta}{\Delta\beta}\right)\Pi\left(\frac{\gamma_\alpha-\gamma}{\Delta\gamma}\right), \tag{13}$$

with the relation ($\alpha \neq \beta \neq \gamma$).

The microscopic transport Eqs. (10)–(13) can allow for the derivation of the transport quantities required for atomic and molecular hydrodynamics, thus yielding the kinetic and configurational contributions of the atoms and molecules based on the first and second terms of Eqs. (11)–(13), respectively. The determination of the atomic and molecular influences on the transport quantities is critical, and the first and second terms are generally evaluated as the ensemble-averaged values of $\langle P_{\alpha\beta}\rangle$ and $\langle J_\alpha\rangle$ in molecular dynamics simulations, respectively [2,3,14]. The pressure tensor and heat flux in Eqs. (11) and (12) represent the local and instantaneous values of the field quantity. However, the influences of the single-particle movement and the single interaction between particles are included in the summation at the point $\mathbf{r}$, which does not allow for the separate influences of a single particle or a single interaction in a condensed phase to be obtained. Relating the field quantities at the atomic scale to the influence of the single-particle movement and the single interaction between particles is necessary for the interpretation of the microscopic field quantities from a more fundamental aspect.

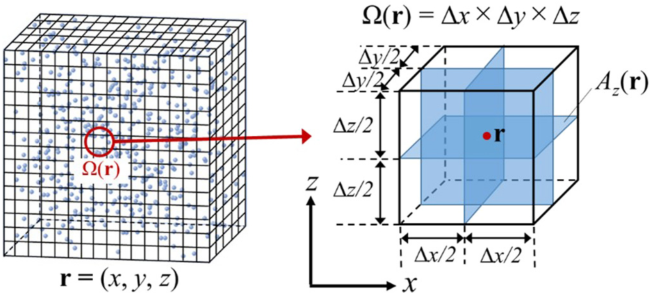

FIG. 1. Definition of the local volume element. The atomic-molecular system is divided into small volume elements (left), and the plane components in the local volume are defined (right).

To more precisely examine a set of the microscopic field quantities of the mass flux, pressure tensor, and heat flux at $(\mathbf{r},t)$ in the system, namely, $(M_\alpha(\mathbf{r},t), P_{\alpha\beta}(\mathbf{r},t), J_\alpha(\mathbf{r},t))$, the density-of-states distribution is considered:

$$\chi^{(\mathbf{r},t)}(\mathbf{X}^n), \tag{14}$$

where the density distribution $\chi^{(\mathbf{r},t)}$ is defined at the space of the variables, and $\mathbf{X}^n$ indicates a set of all variables related to the transport quantities at $(\mathbf{r},t)$, described as

$$\mathbf{X}^n = \overbrace{(\hat{\Psi};\ \hat{\mathbf{r}},\ \hat{\mathbf{v}}, \hat{e}, \ldots)}^{n}, \tag{15}$$

with

$$\hat{\Psi} = (\hat{m}_\alpha,\ \hat{\sigma}_{\alpha\beta,1}, \hat{\sigma}_{\alpha\beta,2},\ \hat{j}_{\alpha,1},\ \hat{j}_{\alpha,2}). \tag{16}$$

In Eq. (16), $\hat{m}_\alpha$, $\hat{\sigma}_{\alpha\beta,1}$, $\hat{\sigma}_{\alpha\beta,2}$, $\hat{j}_{\alpha,1}$, and $\hat{j}_{\alpha,2}$ are the quantities detected at $(\mathbf{r},t)$ by the single-particle movement and single interaction between particles, which are related via the kinetic and configurational parts in Eqs. (10)–(12) as follows:

$$M_\alpha(\mathbf{r},t) = \sum_\xi \sum_{i(\lambda_1\neq 0)} \hat{m}_\alpha, \tag{17}$$

$$\begin{aligned} P_{\alpha\beta}(\mathbf{r},t) &= P_{\alpha\beta,1}(\mathbf{r},t) + P_{\alpha\beta,2}(\mathbf{r},t) \\ &= \sum_\xi \sum_{\substack{i \\ (\lambda_1\neq 0)}} \hat{\sigma}_{\alpha\beta,1} + \sum_\xi\sum_\zeta \sum_{\substack{i,j(\neq i) \\ (\lambda_2\neq 0)}} \hat{\sigma}_{\alpha\beta,2}, \end{aligned} \tag{18}$$

$$\begin{aligned} J_\alpha(\mathbf{r},t) &= J_{\alpha,1}(\mathbf{r},t) + J_{\alpha,2}(\mathbf{r},t) \\ &= \sum_\xi \sum_{\substack{i \\ (\lambda_1\neq 0)}} \hat{j}_{\alpha,1} + \sum_\xi\sum_\zeta \sum_{\substack{i,j(\neq i) \\ (\lambda_2\neq 0)}} \hat{j}_{\alpha,2}, \end{aligned} \tag{19}$$

where

$$\hat{m}_\alpha = \frac{1}{A_\alpha} m_{\xi,i}[\hat{v}_{\xi,i,\alpha} - v_\alpha(\mathbf{r}_{\xi,i},t)]\lambda_1, \tag{20}$$

$$\hat{\sigma}_{\alpha\beta,1} = \frac{1}{A_\alpha} m_{\xi,i}[\hat{v}_{\xi,i,\alpha} - v_\alpha(\mathbf{r}_{\xi,i},t)][\hat{v}_{\xi,i,\beta} - v_\beta(\mathbf{r}_{\xi,i},t)]\lambda_1, \tag{21}$$

$$\hat{\sigma}_{\alpha\beta,2} = -\frac{1}{4A_\alpha}\hat{F}_{\xi i,\zeta j,\beta}\lambda_2, \tag{22}$$

$$\hat{j}_{\alpha,1} = \frac{1}{A_\alpha}\hat{e}_{\xi,i}[\hat{v}_{\xi,i,\alpha} - \bar{v}_\alpha(\mathbf{r}_{\xi,i},t)]\lambda_1, \tag{23}$$

$$\hat{j}_{\alpha,2} = -\frac{1}{4A_\alpha}\hat{\mathbf{F}}_{\xi i,\zeta j}\cdot[\hat{\mathbf{v}}_\xi - \bar{\mathbf{v}}(\mathbf{r},t)]\lambda_2. \tag{24}$$

In Eqs. (20)–(24), λ_1 and λ_2 are defined respectively as

$$\lambda_1 = \delta(\alpha_{\xi,i} - \alpha)\Pi((\beta_{\xi,i} - \beta)/\Delta\beta)\Pi((\gamma_{\xi,i} - \gamma)/\Delta\gamma)$$

and

$$\lambda_2 = [\mathrm{sgn}(\alpha - \alpha_{\xi,i}) - \mathrm{sgn}(\alpha - \alpha_{\zeta,j})] \times \Pi((\beta_\alpha - \beta)/\Delta\beta)\Pi((\gamma_\alpha - \gamma)/\Delta\gamma).$$

In Eq. (15), we consider $\hat{\Psi}$ as a set of the fundamental variables, and $\hat{\mathbf{r}}$, $\hat{\mathbf{v}}$, and $\hat{e}$ are the quantities used to obtain $\hat{m}_\alpha$, $\hat{\sigma}_{\alpha\beta,1}$, $\hat{\sigma}_{\alpha\beta,2}$, $\hat{j}_{\alpha,1}$, and $\hat{j}_{\alpha,2}$ in Eqs. (20)–(24). Assuming the n-dimensional small volume $d\mathbf{X}^n$, the number of states in the range of $\mathbf{X}^n$~$\mathbf{X}^n + d\mathbf{X}^n$ is defined as $\chi^{(\mathbf{r},t)}(\mathbf{X}^n)\,d\mathbf{X}^n$. Then the sum of the states at $(\mathbf{r},t)$ can be obtained as

$$\int_{-\infty}^{\infty}\cdots\int_{-\infty}^{\infty}\chi^{(\mathbf{r},t)}(\mathbf{X}^n)\,d\mathbf{X}^n, = \int_{-\infty}^{\infty}\cdots\int_{-\infty}^{\infty}\chi^{(\mathbf{r},t)}(\hat{\Psi};\mathbf{r},\ldots)\,d\hat{\Psi}\,d\mathbf{r}\ldots \tag{25}$$

with

$$d\hat{\Psi} = d\hat{m}_\alpha\,d\hat{\sigma}_{\alpha\beta,1}\,d\hat{\sigma}_{\alpha\beta,2}\,d\hat{j}_{\alpha,1}\,d\hat{j}_{\alpha,2}. \tag{26}$$

Integrating the other $n - n_{\hat{\Psi}}$ variables yields the following:

$$\int_{-\infty}^{\infty}\cdots\int_{-\infty}^{\infty}\chi^{(\mathbf{r},t)}(\hat{\Psi};\mathbf{X}^{n-n_{\hat{\Psi}}})\,d\mathbf{X}^{n-n_{\hat{\Psi}}} = \Gamma^{(\mathbf{r},t)}(\hat{\Psi}). \tag{27}$$

Here $\Gamma^{(\mathbf{r},t)}$ is used as a distribution function when selecting specific variables, and $\Gamma^{(\mathbf{r},t)}(\hat{\Psi})$ is the density distribution in the space of variables $\hat{m}_\alpha$, $\hat{\sigma}_{\alpha\beta,1}$, $\hat{\sigma}_{\alpha\beta,2}$, $\hat{j}_{\alpha,1}$, and $\hat{j}_{\alpha,2}$. To relate this to the microscopic field quantities, the following expression is used for convenience:

$$\Gamma^{(\mathbf{r},t)}_{\hat{Y}}(\hat{\Psi}) \equiv \hat{Y}(\hat{\Psi})\Gamma^{(\mathbf{r},t)}(\hat{\Psi}), \quad \hat{Y} = \hat{m}_\alpha,\ \hat{\sigma}_{\alpha\beta,1}, \hat{\sigma}_{\alpha\beta,2},\ \hat{j}_{\alpha,1},\ \text{or}\ \hat{j}_{\alpha,2}. \tag{28}$$

The transport quantity at $(\mathbf{r},t)$ is obtained in the general form

$$Y = \int_{-\infty}^{\infty}\cdots\int_{-\infty}^{\infty}\Gamma^{(\mathbf{r},t)}_{\hat{Y}}(\hat{\Psi})\,d\hat{\Psi}. \tag{29}$$

Equation (29) can then be expressed using the specific variables, as follows:

$$\begin{aligned} M_\alpha(\mathbf{r},t) &= \int_{-\infty}^{\infty}\cdots\int_{-\infty}^{\infty}\Gamma^{(\mathbf{r},t)}_{\hat{m}_\alpha}(\hat{\Psi})\,d\hat{\Psi},\\ P_{\alpha\beta}(\mathbf{r},t) &= \int_{-\infty}^{\infty}\cdots\int_{-\infty}^{\infty}\Gamma^{(\mathbf{r},t)}_{\hat{\sigma}_{\alpha\beta,1}}(\hat{\Psi})\,d\hat{\Psi}\\ &\quad + \int_{-\infty}^{\infty}\cdots\int_{-\infty}^{\infty}\Gamma^{(\mathbf{r},t)}_{\hat{\sigma}_{\alpha\beta,2}}(\hat{\Psi})\,d\hat{\Psi},\\ J_\alpha(\mathbf{r},t) &= \int_{-\infty}^{\infty}\cdots\int_{-\infty}^{\infty}\Gamma^{(\mathbf{r},t)}_{\hat{j}_{\alpha,1}}(\hat{\Psi})\,d\hat{\Psi}\\ &\quad + \int_{-\infty}^{\infty}\cdots\int_{-\infty}^{\infty}\Gamma^{(\mathbf{r},t)}_{\hat{j}_{\alpha,2}}(\hat{\Psi})\,d\hat{\Psi}. \end{aligned} \tag{30}$$

For the local transport quantity between the contacting layers, $\Gamma^{(\mathbf{r},t)}(\hat{\Psi})$ is transformed into the following:

$$\Gamma^{(\mathbf{r},t)}(\hat{\Psi}) = \Gamma^{(\mathbf{r},t)}(\hat{\sigma}_{\alpha\beta,2},\hat{j}_{\alpha,2}). \tag{31}$$

The first terms in the transport equations [Eqs. (18) and (19)] can be ignored when only the transport across the interface is considered, because there exist no atoms or molecules between the contacting layers. The subscript of the variable is simplified as follows:

$$\hat{\sigma}_{\alpha\beta,2} \to \hat{\sigma}_{\alpha\beta}, \quad \hat{j}_{\alpha,2} \to \hat{j}_\alpha, \tag{32}$$

which yields the expressions

$$\begin{aligned} P_{\alpha\beta}(\mathbf{r},t) &= \int_{-\infty}^{\infty}\Gamma^{(\mathbf{r},t)}_{\hat{\sigma}_{\alpha\beta}}(\hat{\Psi})\,d\hat{\Psi},\\ J_\alpha(\mathbf{r},t) &= \int_{-\infty}^{\infty}\Gamma^{(\mathbf{r},t)}_{\hat{j}_\alpha}(\hat{\Psi})\,d\hat{\Psi}, \end{aligned} \tag{33}$$

where

$$\Gamma^{(\mathbf{r},t)}(\hat{\Psi}) = \Gamma^{(\mathbf{r},t)}(\hat{\sigma}_{\alpha\beta},\hat{j}_\alpha). \tag{34}$$

The microscopic quantity of the stress tensor using the density distribution of the single-interaction-based energy flux is

$$\begin{aligned} P_{\alpha\beta}(\mathbf{r},t) &= \int_{-\infty}^{\infty}\int_{-\infty}^{\infty}\hat{\sigma}_{\alpha\beta}\Gamma^{(\mathbf{r},t)}(\hat{\sigma}_{\alpha\beta},\hat{j}_\alpha)\,d\hat{\sigma}_{\alpha\beta}\,d\hat{j}_\alpha\\ &= \int_{-\infty}^{\infty}\int_{-\infty}^{\infty}\Gamma^{(\mathbf{r},t)}_{\hat{\sigma}_{\alpha\beta}}(\hat{\sigma}_{\alpha\beta},\hat{j}_\alpha)\,d\hat{\sigma}_{\alpha\beta}\,d\hat{j}_\alpha\\ &= \int_{-\infty}^{\infty}\Gamma^{(\mathbf{r},t)}_{\hat{\sigma}_{\alpha\beta}}(\hat{j}_\alpha)\,d\hat{j}_\alpha, \end{aligned} \tag{35}$$

where $\Gamma^{(\mathbf{r},t)}_{\hat{\sigma}_{\alpha\beta}}(\hat{j}_\alpha)$ is the 1D density distribution multiplied by $\hat{\sigma}_{\alpha\beta}$, which is dependent on the single-interaction-based energy flux $\hat{j}_\alpha$, indicating the contributions of the single-interaction-based energy flux to the local and instantaneous expression of the microscopic quantity $P_{\alpha\beta}(\mathbf{r},t)$. Similarly, we obtain

$$\begin{aligned} J_\alpha(\mathbf{r},t) &= \int_{-\infty}^{\infty}\int_{-\infty}^{\infty}\hat{j}_\alpha\Gamma^{(\mathbf{r},t)}(\hat{\sigma}_{\alpha\beta},\hat{j}_\alpha)\,d\hat{j}_\alpha\,d\hat{\sigma}_{\alpha\beta}\\ &= \int_{-\infty}^{\infty}\int_{-\infty}^{\infty}\Gamma^{(\mathbf{r},t)}_{\hat{j}_\alpha}(\hat{\sigma}_{\alpha\beta},\hat{j}_\alpha)\,d\hat{j}_\alpha\,d\hat{\sigma}_{\alpha\beta}\\ &= \int_{-\infty}^{\infty}\Gamma^{(\mathbf{r},t)}_{\hat{j}_\alpha}(\hat{\sigma}_{\alpha\beta})\,d\hat{\sigma}_{\alpha\beta}, \end{aligned} \tag{36}$$

where $\Gamma^{(\mathbf{r},t)}_{\hat{j}_\alpha}(\hat{\sigma}_{\alpha\beta})$ is the density distribution multiplied by $\hat{j}_\alpha$, which is dependent on the single-interaction-based stress tensor $\hat{\sigma}_{\alpha\beta}$. Equations (35) and (36) are based on the relationships

$P_{\alpha\beta}(\mathbf{r},t) = \Sigma P_{\alpha\beta,2}$ and $J_\alpha(\mathbf{r},t) = \Sigma J_{\alpha,2}$, which hold for the interface between the contacting regions.

In the 2D distribution, the energy flux in the $\hat{\sigma}_{\alpha\beta} - \hat{Z}$ plane can be obtained as

$$\Gamma^{(\mathbf{r},t)}_{\hat{j}_\alpha}(\hat{\sigma}_{\alpha\beta}, \hat{Z}) = \int_{-\infty}^{\infty} \cdots \int_{-\infty}^{\infty} \Gamma^{(\mathbf{r},t)}_{\hat{j}_\alpha}(\hat{\sigma}_{\alpha\beta}, \hat{Z}, \mathbf{X}^{n-n_{\hat{\sigma}_{\alpha\beta},\hat{Z}}})\, d\mathbf{X}^{n-n_{\hat{\sigma}_{\alpha\beta},\hat{Z}}}, \quad (37)$$

where

$$\Gamma^{(\mathbf{r},t)}_{\hat{j}_\alpha}(\hat{\sigma}_{\alpha\beta}, \hat{Z}, \mathbf{X}^{n-n_{\hat{\sigma}_{\alpha\beta},\hat{Z}}}) = \hat{J}_\alpha \Gamma^{(\mathbf{r},t)}(\hat{\sigma}_{\alpha\beta}, \hat{Z}, \mathbf{X}^{n-n_{\hat{\sigma}_{\alpha\beta},\hat{Z}}}). \quad (38)$$

In Eqs. (37) and (38), a variable $\hat{Z}$ is chosen—which corresponds, for instance, to the position, velocity, energy, or temperature of the particle—to understand the transport quantities with respect to the single interaction. In Eq. (15) we defined a set of variables composed of the fundamental transport quantities using the single-particle movement and single interaction between particles in addition to related quantities. For clear interpretation, it should be noted that the variables (e.g., $\hat{\mathbf{v}}$) in Eq. (15) are defined as the quantities when $\hat{\sigma}_{\alpha\beta}$ or $\hat{j}_\alpha$ are observed at $(\mathbf{r}, t)$ in the system and do not signify the field quantity itself at $(\mathbf{r}, t)$.

For a solid-liquid interface, the second term on the right-hand side of Eq. (24) is equal to the heat flux as expressed by Eq. (32). In a steady state without a streaming velocity, it is known that the following relationship can be obtained [24]:

$$\frac{1}{2}\sum_{j\in l}\sum_{i\in s}\langle \mathbf{F}_{ij}\cdot(\mathbf{v}_i + \mathbf{v}_j)\rangle = \sum_{j\in l}\sum_{i\in s}\langle \mathbf{F}_{ij}\cdot\mathbf{v}_i\rangle, \quad (39)$$

which holds for the energy transport across the interface, where l and s represent the liquid and solid, respectively. In the above relation, <> denotes the ensemble average. For the single-interaction-based energy flux across the interface, we used the following expression to evaluate the single-interaction-based energy flux in this study:

$$\hat{j}_{\alpha,2} = -\frac{1}{2A_\alpha}\hat{\mathbf{F}}_{sl}\cdot(\hat{\mathbf{v}}_s + \hat{\mathbf{v}}_l), \quad (40)$$

with the corresponding stress,

$$\hat{\sigma}_{\alpha\beta,2} = -\frac{1}{A_\alpha}F_{\beta,sl}. \quad (41)$$

In Appendix B the thermal transport across a solid-liquid interface is detailed using the expression of $\mathbf{F}_{ij}\cdot\mathbf{v}_i$ presented in Eq. (24): $\hat{j}_{\alpha,2} = -(1/A_\alpha)\hat{\mathbf{F}}_{sl}\cdot\hat{\mathbf{v}}_s$.

III. NUMERICAL DETAILS

To calculate the 3D heat flux in a solid-liquid interfacial region, we adopt a model in which monatomic molecules are present in a liquid state between two planar solid walls. As detection of the 3D heat flux requires significant computation resources, we use relatively small system dimensions of $L_x \times L_y \times L_z = 3.23 \times 3.23 \times 4.20\,\mathrm{nm}^3$. The two walls are located at the lower and upper sides in the z direction of the system, and a temperature gradient is imposed between the two walls. Periodic boundary conditions are imposed in the x and y directions. The interactions between the liquid-liquid and solid-solid particles are assumed to be described by the 12-6 Lennard-Jones (LJ) potential function. The form of the liquid-liquid interaction is described as $\phi_{ff}(r_{ij}) = 4\varepsilon_{ff}[(\sigma_{ff}/r_{ij})^{12} - (\sigma_{ff}/r_{ij})^6]$ with the subscript ff. Here r_{ij} is the distance between the ith and jth particles, and σ_{ff} and ε_{ff} are 3.405 Å and 1.67×10^{-21} J, respectively, as the parameters of argon (Ar) molecules. Hereafter, the normalized values based on the standard LJ parameters of Ar molecules are used. The values of $\sigma_{ss} = 0.746$ and $\varepsilon_{ss} = 65.39$ are selected as the parameters of platinum (Pt) atoms for the solid-solid atom interactions [31]. For the solid-liquid interactions, an LJ potential function is used, namely, $\phi_{fs}(r_{ij}) = 4\varepsilon_{fs}[(\sigma_{fs}/r_{ij})^{12} - (\sigma_{fs}/r_{ij})^6]$ with the parameter ε_{fs}, where σ_{fs} is obtained using the Lorentz-Berthelot rule, and ε_{fs} is varied within the range of $0.5 \leqslant \varepsilon_{fs} \leqslant 2.0$ [32]. The cutoff distance is set as 2.5. Each solid wall consists of five layers with the (100) plane facing the liquid phase, and the temperature of the walls is controlled using the Langevin method at the second layer facing the outermost fixed layers in the system. With the objective of detecting the 3D heat flux at the single-atom scale in the solid-liquid interfacial region, the temperatures of the upper and lower solids are set to $T^* = T/(\varepsilon_{ff}/k_B) = 0.41$ and 1.24, respectively, where k_B is the Boltzmann constant; this generates a large temperature gradient. The average pressure $[P^* = P/(\varepsilon_{ff}/\sigma_{ff}{}^3)]$ is 1.18 in the simulations. The simulations are conducted with a time step of $\Delta t^* = t/[\sigma_{ff}(m_f/\varepsilon_{ff})^{1/2}] = 9.3 \times 10^{-4}$, and the equation of motion is numerically integrated using the velocity Verlet method. For simplicity, the asterisk superscript is omitted hereafter. The validation of the simulation conditions (i.e., model size and cutoff distance) is presented in Appendix A.

With respect to the initial conditions, the temperature of the liquid is set to 0.82 using the velocity-scaling method, and the simulation is conducted for 1.0×10^5 time steps. Then the relaxation calculation without controlling the liquid temperature is conducted for 0.1×10^9 time steps. Thereafter, the physical quantities are calculated at a resolution of $dx \times dz = 0.03 \times 0.03$ in the x-z plane to obtain the 2D heat flux distribution, whereas $dx \times dy = 0.059 \times 0.059$ in the x-y plane is adopted to obtain the 3D heat flux distribution. The values obtained are averaged over 5.0×10^9 time steps in the absence of specific description.

In general, detecting the heat flux as a meaningful value at the subatomic scale is difficult owing to the high computational load. To estimate the required time, let us introduce $\tilde{\tau}_\Lambda(q)$ as the characteristic time to observe the 1D heat flux at the steady state in the system with the macroscopic heat flux q, where the area of the system normal to the q is defined as Λ. In common molecular dynamics simulations of condensed matter, $\tilde{\tau}_\Lambda(q)$ can be estimated as several nanoseconds under a large temperature gradient for a system where Λ has an area of several square nanometers. The characteristic time $\tilde{\tau}_A$ required to detect the heat flux at the local area A in the system is then proportional to the ratio of the overall area Λ to the local area

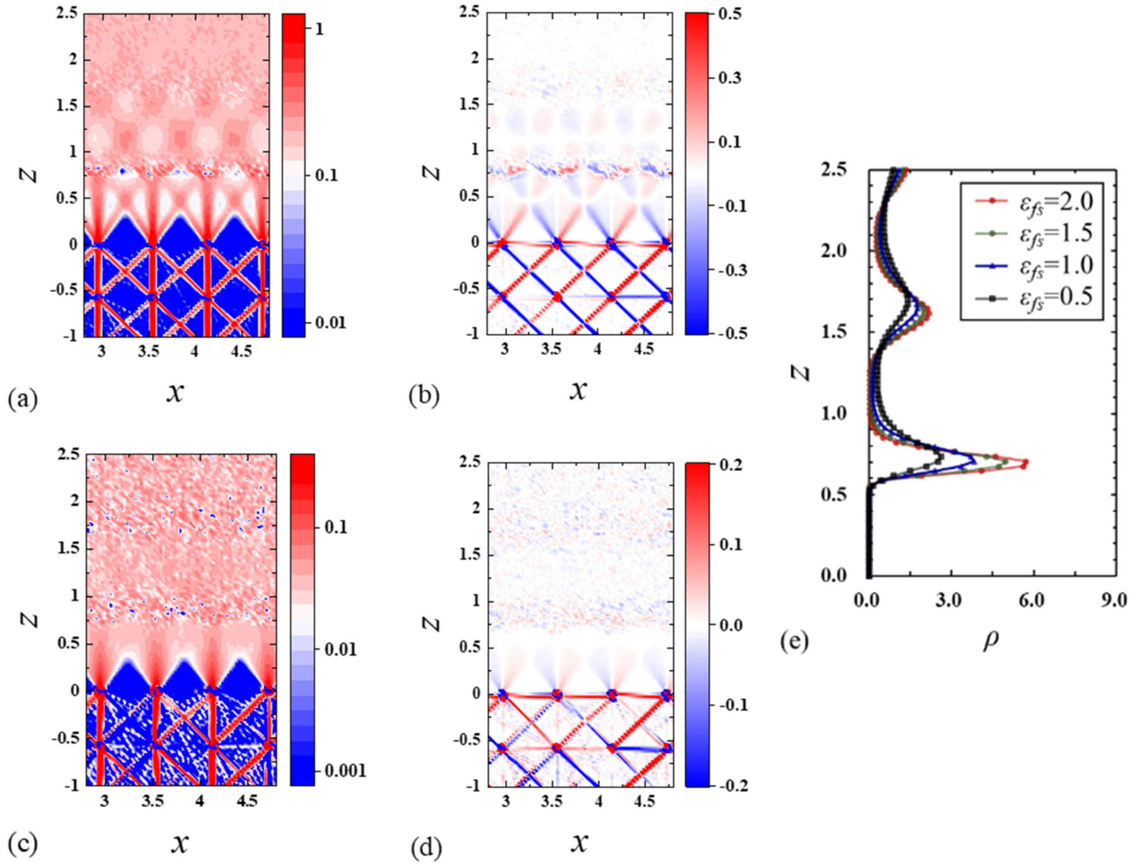

FIG. 2. Two-dimensional heat flux at a solid-liquid surface: (a) $\langle J_z \rangle$ ($\varepsilon_{fs} = 2.0$), (b) $\langle J_x \rangle$ ($\varepsilon_{fs} = 2.0$), (c) $\langle J_z \rangle$ ($\varepsilon_{fs} = 0.5$), and (d) $\langle J_x \rangle$ ($\varepsilon_{fs} = 0.5$); where $\langle J_z \rangle$ and $\langle J_x \rangle$ represent the z and x components of the heat flux, respectively. The upper ($z \gtrsim 0.7$) and lower ($z \leqslant -0.09$) regions are the liquid and solid phases, respectively. (e) Values of ρ: 1D density distribution of the fluid molecules in the z direction, for $\varepsilon_{fs} = 0.5$, 1.0, 1.5, and 2.0, where the values are calculated in the slab with a width of $dz = 0.03$. The values are normalized using LJ parameters.

A, and can be obtained as

$$\tilde{\tau}_A = \chi \frac{\Lambda}{A} \tilde{\tau}_\Lambda(q), \tag{42}$$

where χ is the parameter that reflects the properties of the heat flux at the local area. In a homogeneous system at the atomic scale, such as a bulk gas or liquid, χ can be assumed to be equal to 1.0. Contrarily, the influence of the resolution Λ/A adopted in our calculation exceeded 10^4, which indicates that more than $10\,\mu$s is required to detect the heat flux at the subatomic scale in molecular simulations. Furthermore, the influence of the algorithm with respect to obtaining the 3D heat flux and the number of the local volumes needs to be considered to estimate the actual computational costs. These factors increase the difficulty of detecting the heat flux. However, in this study, we focused on a liquid-solid interface (an inhomogeneous system) and detected strong heat fluxes as the time-averaged values over several microseconds, as the parameter χ is less than 1.0 for strong heat fluxes at the subatomic scale in the interfacial region. In the present study, the 3D stress and heat flux are obtained by simulations carried out for 5.0×10^9 time steps ($10\,\mu$s), which is acceptable for the adopted parameters. However, numerical errors should be considered for a significantly low heat flux regime.

IV. TWO-DIMENSIONAL TRANSPORT FIELD AT SUBATOMIC SCALE

Figure 2 presents the 2D heat flux at a solid-liquid interface, including the solid phase located at the lower side of the system. This result is critical to understand the subsequent 3D results. In Fig. 2 the z and x components of the heat flux, namely, $\langle J_z \rangle = \langle J_z(\mathbf{r}, t) \rangle$ and $\langle J_x \rangle = \langle J_x(\mathbf{r}, t) \rangle$, respectively, are presented for $\varepsilon_{fs} = 0.5$ and 2.0, and the macroscopic heat transfer direction is from the lower solid phase ($z \leqslant -0.09$) to the liquid phase ($z \gtrsim 0.7$) in the z direction. Notably, no molecules or atoms are present in the space between the contacting solid and liquid layers ($0.0 < z \lesssim 0.7$). In this study, $\langle J_z \rangle$ and $\langle J_x \rangle$ at both the solid and liquid phases are obtained based on Eq. (12) at a subatomic resolution of $dx \times dz = 0.03 \times 0.03$ and presented as the averaged values over 0.5×10^9 time steps. The representation of $\langle J_z \rangle$ without the solid phase at different thermodynamic states was presented in a previous study [25] and is consistent with the results calculated based on the method presented in this study. The results revealed that the heat flux corresponding to the crystalline solid could be detected in the solid phase ($z \leqslant -0.09$), which is mainly attributed to the strong interactions between the solid atoms. The x direction is not the macroscopic heat transfer direction, and the averaged value along the x direction is equal to zero. However, as shown in Figs. 2(b) and 2(d), $\langle J_x \rangle$ exhibits values at the atomic scale, which is important for more complex interfaces, such as an amorphous surface or a functional interface with atomic structures [26]. As shown in Figs. 2(a) and 2(c), at $z \leqslant -0.09$, the strong heat fluxes (red lines) intersect the positions of the solid atoms; however, the heat flux at this position is difficult to detect because of the high-frequency vibrations of the solid atoms, which requires an extremely high spatial resolution. Moreover, the heat flux in the liquid phase ($z \gtrsim 0.7$) reflects the structure of the liquid adsorbed layers in contact with the solid surface. Focusing on the space between the adjacent solid-liquid layers, a nonuniform heat flux along the macroscopic temperature gradient can be observed, and the influence is significant in the case of strong interaction strength. This directional quality is a key factor in enhancing the thermal transport at the single-atom scale [26].

V. THREE-DIMENSIONAL TRANSPORT FIELD AT SUBATOMIC SCALE

In this section, 3D field quantities such as the stress and heat flux at a solid-liquid interface, as obtained at a subatomic scale resolution, are presented, and nonuniform transport properties between the contacting liquid-solid layers are examined. The influence of the solid-liquid interaction strength on the local transport quantities is investigated, and the 3D transport field is compared with the 2D transport field. Furthermore, the correlation between the heat flux and stress at the subatomic scale is investigated.

The 3D heat flux at a solid-liquid interface is calculated based on Eq. (12) with a subatomic resolution of $dx \times dy = 0.059 \times 0.059$ and obtained as the time-averaged value for 5.0×10^9 time steps (10.0 μs). The x, y, and z components of the heat flux, namely, $\langle J_x \rangle = \langle J_x(\mathbf{r}, t) \rangle$, $\langle J_y \rangle = \langle J_y(\mathbf{r}, t) \rangle$, and $\langle J_z \rangle = \langle J_z(\mathbf{r}, t) \rangle$, respectively, for $\varepsilon_{fs} = 2.0$ and 0.5, are shown, respectively, in Figs. 3 and 4, in the x-y plane at each z position between the adjacent solid-liquid layers ($-0.09 < z \lesssim 0.7$). In addition, the density distributions at the contacting solid and liquid layers are shown in Figs. 3(d) and 4(d). Based on the results in Fig. 3(c), the directional heat fluxes from each solid atom comprising the solid surface are detected, and the fluxes are broadened and decayed closer to the liquid phase boundary ($z \approx 0.7$). The heat flux from a surface solid atom is composed of four directional heat fluxes, and under hydrophilic conditions, strong directional heat fluxes can be detected even in the immediate vicinity of the liquid phase [Fig. 3(c): $\varepsilon_{fs} = 2.0$ and $z = 0.41$]. This is due to the high density of the liquid molecules shown in Fig. 3(d) ($z = 0.7$), which can be understood from the results of $\langle J_x \rangle$ and $\langle J_y \rangle$ in Figs. 3(a) and 3(b), where the heat flux directions are toward the high-density sites of the liquid molecules. These results may be considered as direct evidence of the thermal transport enhancement of a hydrophilic surface. Moreover, the directional qualities are weak in the case of $\varepsilon_{fs} = 0.5$, as shown in Fig. 4, where the thermal conductance is lower than that of $\varepsilon_{fs} = 2.0$. These results indicate that the 3D heat flux at the atomic scale reflects the structure of the liquid-adsorbed layer facing the solid surface atoms, which provides critical information based on atomic-scale transport properties to determine the thermal transport mechanisms and modulate thermal conductance at a solid-liquid interface.

Figures 5 and 6 present the stress fields corresponding to the heat flux in Figs. 3 ($\varepsilon_{fs} = 2.0$) and 4 ($\varepsilon_{fs} = 0.5$), respectively, in which the stress tensors of $\langle P_{xx} \rangle$, $\langle P_{yy} \rangle$, and $\langle P_{zz} \rangle$ are shown. The 3D stress field at a solid-liquid interface is calculated based on Eq. (11). The stress field exhibits the same trend as the heat flux; the directional quality weakens when it approaches the liquid ($z = 0.7$). However, negative values can be detected, which are more complex in the x-y plane compared with the heat flux results in Figs. 3 and 4. As is clear from the comparison of Figs. 3–6, the thermal transport properties, including directional qualities, are correlated with the properties of stress at the subatomic scale, especially in the z component. The strong heat fluxes correspond to high stresses in the x-y plane. The details of the heat flux and stress at $y = 3.5$ in the x direction are summarized in Figs. 7(a) and 7(b), respectively, for $\varepsilon_{fs} = 0.5$, 1.0, 1.5, and 2.0, from which we can confirm the relationship between the heat flux and the stress fields.

Figure 8 presents the maximum value of the 3D heat flux at each z-component along the macroscopic temperature gradient (z direction), which is significantly related to the directional qualities of the detected heat flux. In Fig. 8 the values are normalized using the values of the 1D heat flux for each case of ε_{fs}, and the 2D heat flux at $x = 3.52$ from Fig. 2(a) is plotted. The results reveal that the 1D, 2D, and 3D heat fluxes are significantly different in the region of the contacting layers ($-0.09 < z < 0.7$), which indicates that the 3D heat flux should be evaluated to quantitatively determine the heat flux properties at the single-atom scale. For example, at $z = 0.41$ in the immediate vicinity of the contacting liquid layer, the maximum value of the 3D heat flux ($\varepsilon_{fs} = 0.5$) exceeds that of the 1D flux by a factor of three. The maximum values of the heat flux from the solid atoms decay with an increase in the distance from the surface, which suggests that modulating this property is a potential method of modulating thermal transport across the interface.

The macroscopic heat flux and stress in the z direction (temperature gradient direction) at the interface are expressed using the local and instantaneous quantities in Eqs. (11) and (12), as follows:

$$J_z^{\mathrm{macro}} = \frac{1}{\bar{A}} \iint \langle J_z(\mathbf{r}, t) \rangle dA, \tag{43}$$

$$P_{zz}^{\mathrm{macro}} = \frac{1}{\bar{A}} \iint \langle P_{zz}(\mathbf{r}, t) \rangle dA, \tag{44}$$

where $\bar{A}$ and $dA = A_z(\mathbf{r})$ represent the overall and local interfacial areas perpendicular to the z direction, respectively (Fig. 1). Following Eqs. (43) and (44), the interfacial thermal conductance (ITC) at a macroscopic pressure is

$$C^{\mathrm{macro}}|_{P_{zz}^{\mathrm{macro}}} = \frac{J_z^{\mathrm{macro}}}{\Delta T}, \tag{45}$$

where the temperature jump at the interface is ΔT. Hence, we obtain the following operationally defined expression by

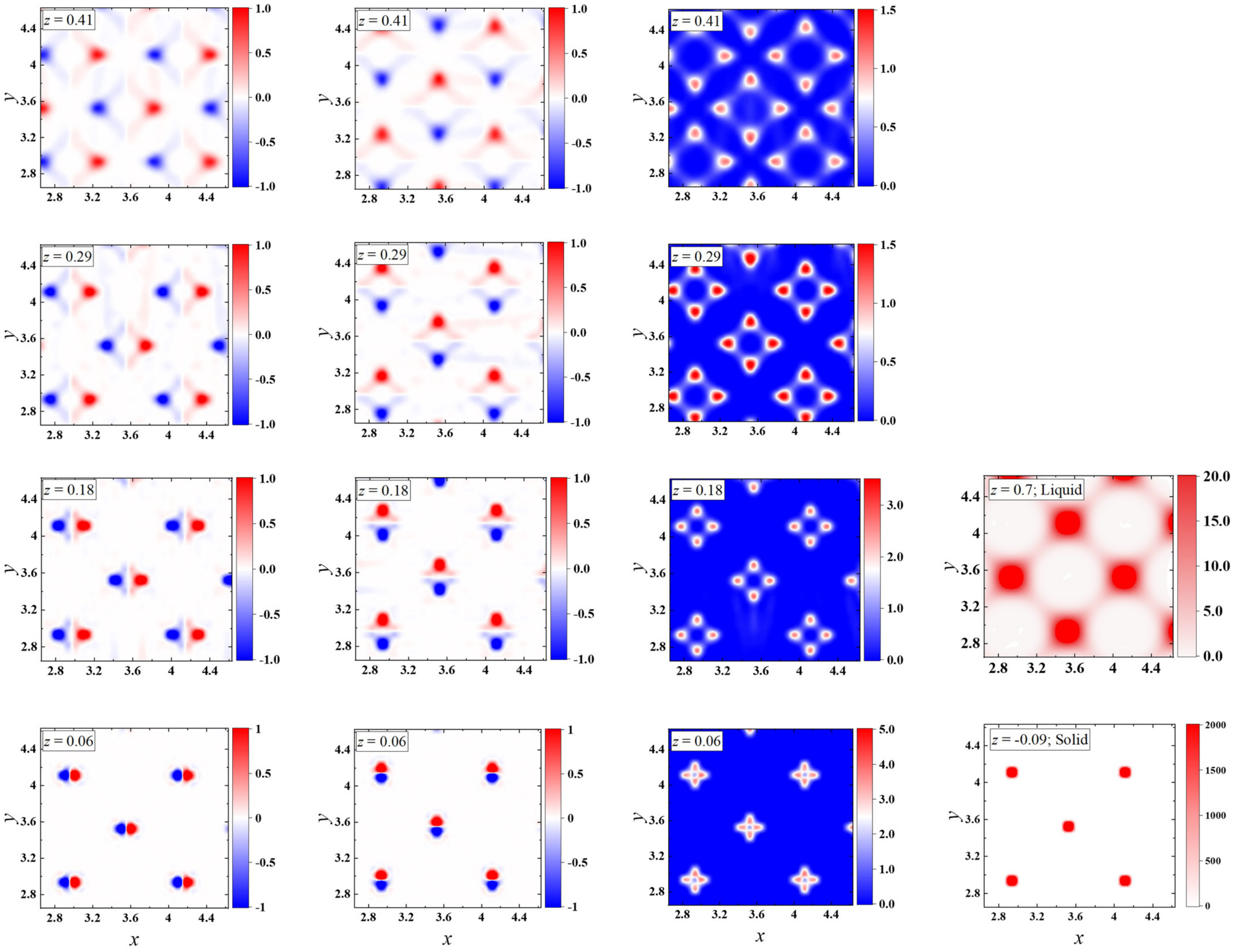

(a) $< J_x >$ (b) $< J_y >$ (c) $< J_z >$ (d) $< \rho >$

FIG. 3. Three-dimensional heat flux at the solid-liquid interface for $\varepsilon_{fs} = 2.0$. Panels (a)–(c) present the x, y, and z components of the heat flux, namely, $\langle J_x\rangle$, $\langle J_y\rangle$, and $\langle J_z\rangle$, respectively, which are calculated at $z = 0.06$, 0.18, 0.29, and 0.41 between the contacting solid and liquid layers. Panel (d) presents the density distributions of the solid atoms at the solid surface ($z = -0.09$) and those of the liquid molecules at the liquid layer ($z = 0.7$) in the case of $\varepsilon_{fs} = 2.0$. The density distributions are calculated in the x-y plane with the width $dz = 0.059$. The values are normalized using the LJ parameters.

assuming that the local ITC as $C^{\mathrm{macro}} = \frac{1}{A}\iint \langle C(\mathbf{r},t)\rangle dA$:

$$\frac{1}{A}\iint \langle C(\mathbf{r},t)\rangle\, dA\bigg|_{\frac{1}{A}\iint \langle P_{zz}(\mathbf{r},t)\rangle\, dA} = \frac{\frac{1}{A}\int\int \langle J_z(\mathbf{r},t)\rangle\, dA}{\Delta T} \Rightarrow C(\mathbf{r})|_{P_{zz}(\mathbf{r})} = \frac{J_z(\mathbf{r})}{\Delta T}. \qquad (46)$$

We assume that the thermal transport is 1D (z axis), and the interface is flat, which ensures a 1D temperature gradient in the system. In Eq. (46) we use $C(\mathbf{r}) = \langle C(\mathbf{r},t)\rangle$, $P_{zz}(\mathbf{r}) = \langle P_{zz}(\mathbf{r},t)\rangle$, and $J_z(\mathbf{r}) = \langle J_z(\mathbf{r},t)\rangle$. The local ITC from the macroscopic concept in Eq. (46) indicates that the local interfacial thermal conductance should be understood by considering the condition of the local stress.

To reveal the correlation between the local stress and the heat flux, Fig. 9 presents the relationship between the heat flux and stress at $z = 0.41$, for $\varepsilon_{fs} = 0.5$ [Fig. 9(a)], 1.0 [Fig. 9(b)], 1.5 [Fig. 9(c)], and 2.0 [Fig. 9(d)]. As can be seen in each figure, the heat flux is proportional to the stress, especially in the case of positive stress, and the negative stress detected in Figs. 5 and 6 does not predominantly contribute to the net heat flux. Several negative heat fluxes are plotted in Fig. 9, the mechanism of which is discussed in Sec. VI. Hence, based on this result, the relationship between the time-averaged local heat flux and stress is obtained using the constant coefficient L:

$$\langle J_z(\mathbf{r},t)\rangle / \langle P_{zz}(\mathbf{r},t)\rangle = L. \qquad (47)$$

This relation is independent on the location $\mathbf{r}$ in the x-y plane. The results of the gradient obtained from the linearly fitted line (L) are summarized in Table I. The gradient is dependent on the solid-liquid interaction strength ε_{fs} and the z axis between the contacting layers at the interface. Based

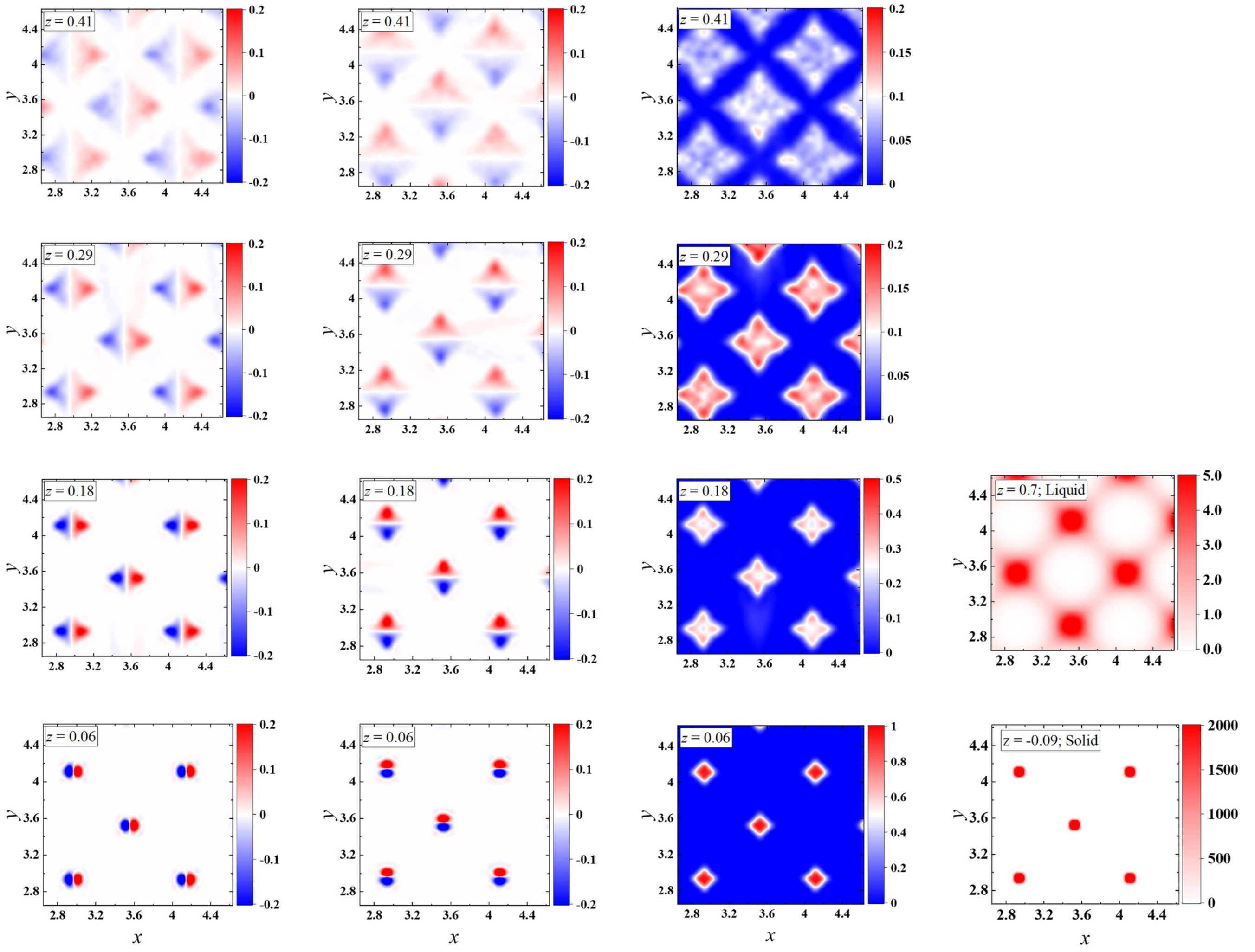

(a) $< J_x >$ (b) $< J_y >$ (c) $< J_z >$ (d) $< \rho >$

FIG. 4. Three-dimensional heat flux at the solid-liquid interface for $\varepsilon_{fs} = 0.5$. Panels (a)–(c) present the x, y, and z components of the heat flux, namely, $\langle J_x \rangle$, $\langle J_y \rangle$, and $\langle J_z \rangle$, respectively, which are calculated at $z = 0.06$, 0.18, 0.29, and 0.41 between the contacting solid and liquid layers. Panel (d) presents the density distributions of the solid atoms at the solid surface ($z = -0.09$), and those of the liquid molecules at the liquid layer ($z = 0.7$) in the case of $\varepsilon_{fs} = 0.5$.

on Eq. (47), the local ITC, as defined by Eq. (46), can be interpreted as follows. Under macroscopic thermodynamic conditions, the ITC reveals the values reflecting the local heat flux, and the changes in the local ITC are mainly caused by stress changes in the corresponding subatomic space.

VI. RELATIONSHIP BETWEEN THE TRANSPORT QUANTITIES AT MACRO- AND SUBATOMIC SCALES BASED ON SINGLE-INTERACTION-BASED STRESS AND ENERGY FLUX

So far we have shown the 3D structure of the stress and heat flux at subatomic resolution in the solid-liquid contacting layers and revealed the relation between the quantities at the macro- and subatomic scales. In this section, we focus on elucidating the thermal transport mechanism from a more fundamental aspect, i.e., in terms of the single-interaction-based stress and energy flux, which bridges the quantities at the macroscopic and subatomic scales. The single-interaction-based stress and energy flux play an important role in understanding the origin of the thermal transport mechanism at the subatomic scale.

Figure 10 presents the time-averaged density-of-states distribution in the plane of the stress and the energy flux due to a single interaction. The results in Fig. 10 are presented for the cases of $\varepsilon_{fs} =$ (a) 0.5 and (b) 2.0, in which the vertical and horizontal axes denote the single-interaction-based stress $\hat{\sigma}_{zz}$ and energy flux $\hat{j}_z$ calculated using Eqs. (41) and (40), respectively. The zz and z components of the stress and energy flux are calculated for the integrated area in the xy plane ($\bar{A}$; $2.6 < x < 4.7$, and $2.6 < y < 4.7$), which reflects the property of the entire interfacial area along the z axis between the contacting solid-liquid layers:

$$\Gamma(\hat{\sigma}_{zz}, \hat{j}_z) = \langle \Gamma^{(t)}(\hat{\sigma}_{zz}, \hat{j}_z) \rangle = \left\langle \sum_{\mathbf{r} \in \bar{A}} \Gamma^{(\mathbf{r},t)}(\hat{\sigma}_{zz}, \hat{j}_z) \right\rangle. \quad (48)$$

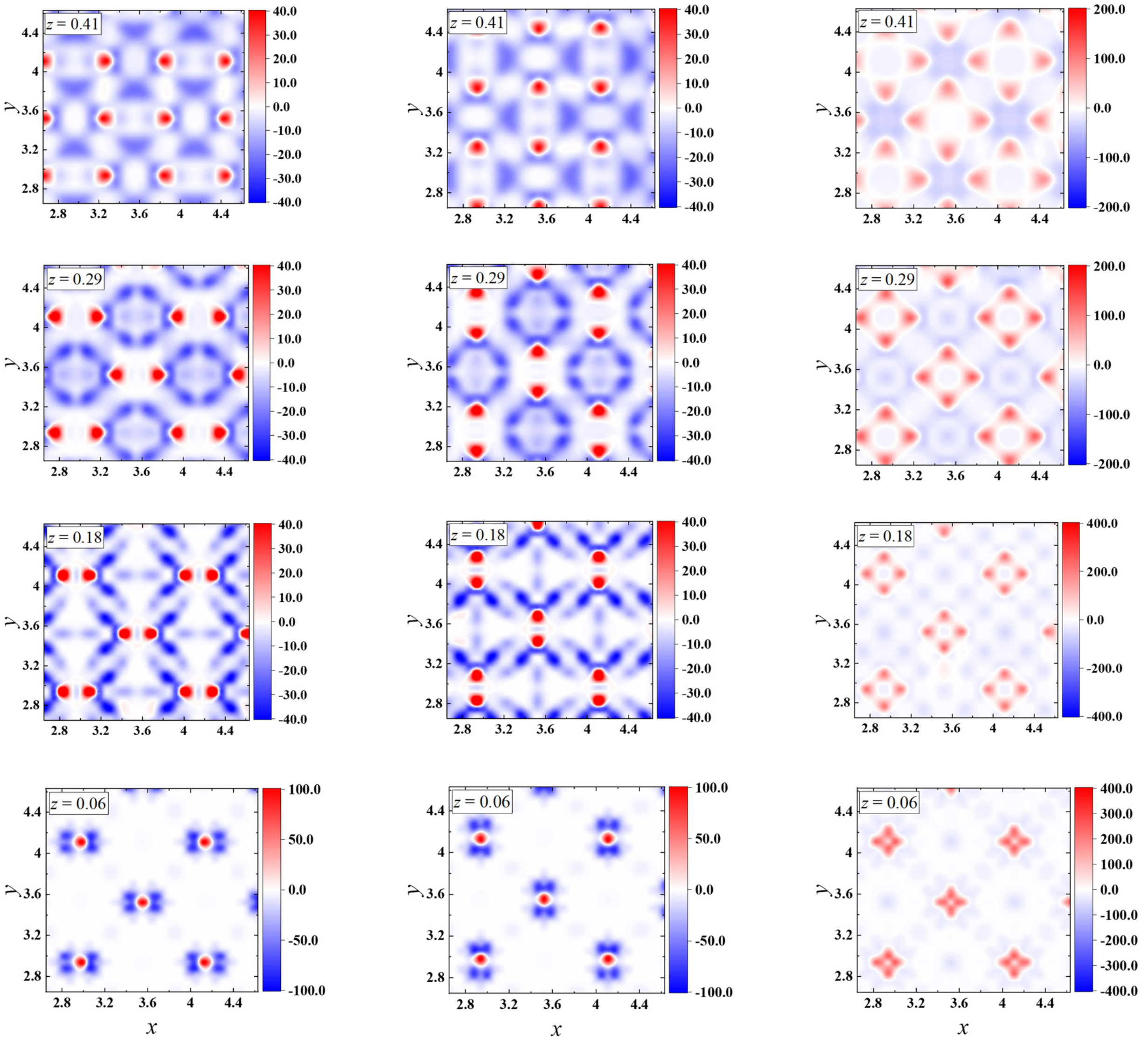

(a) $< P_{xx} >$ (b) $< P_{yy} >$ (c) $< P_{zz} >$

FIG. 5. Three-dimensional stress at the solid-liquid interface for $\varepsilon_{fs} = 2.0$. Panels (a)–(c) present the *xx*, *yy*, and *zz* components of the stress, namely, $\langle P_{xx}\rangle$, $\langle P_{yy}\rangle$, and $\langle P_{zz}\rangle$, respectively, which are calculated at $z = 0.06$, 0.18, 0.29, and 0.41 between the contacting solid and liquid layers. The values are normalized using the LJ parameters.

Here $\Gamma^{(\mathbf{r},t)}(\hat{\sigma}_{zz}, \hat{j}_z)$ is defined in Eq. (34), and the value is calculated at $\mathbf{r}$ with $A_z(\mathbf{r}) = dx \times dy = 0.059 \times 0.059$. Notably, $\Gamma(\hat{\sigma}_{zz}, \hat{j}_z)$ is not dependent on the z position between the contacting solid-liquid layers because the heat flux is 1D (z axis). Based on the results, a symmetric profile is observed for $\hat{j}_z = 0$ in the horizontal axis. Moreover, we cannot identify a symmetric profile in the stress ($\hat{\sigma}_{zz}$) direction; the density within the negative stress range is higher, and it decreases in the positive stress direction over a wider range of $\hat{j}_z$. As can be seen from Fig. 10, the density within the entire range of $\Gamma(\hat{\sigma}_{zz}, \hat{j}_z)$ increases with an increase in the solid-liquid interaction strength ε_{fs}. The figure presents an image of the macroscopic quantities of the stress tensor and heat flux with respect to the single interaction between liquid molecules and solid atoms, which is critical for relating the transport quantities at the macroscopic and subatomic scales.

To better understand the behavior of $\Gamma(\hat{\sigma}_{zz}, \hat{j}_z)$ in Fig. 10, the density distributions of $\Gamma(\hat{\sigma}_{zz}, \hat{v}_{z,+}) = \langle \Gamma^{(t)}(\hat{\sigma}_{zz}, \hat{v}_{z,+})\rangle$ and $\Gamma_{\hat{j}_z}(\hat{\sigma}_{zz}, \hat{v}_{z,+}) = \langle \Gamma^{(t)}_{\hat{j}_z}(\hat{\sigma}_{zz}, \hat{v}_{z,+})\rangle$ for $\varepsilon_{fs} = 2.0$ are presented in Figs. 11(a) and 11(b) respectively, where $\hat{v}_{z,+}$ is the sum of the z components of the solid-atom and liquid-molecule velocities, and is defined as $\hat{v}_{z,+} = \hat{v}_{z,s} + \hat{v}_{z,l}$. The results are calculated as the spatially and temporally averaged values over the entire interface, in the same manner as in Eq. (48). Furthermore, the values are presented also in the $\hat{\sigma}_{zz} - |\hat{v}_{z,+}|$ plane in Figs. 11(c) and 11(d). The values in the $\hat{\sigma}_{zz} - \hat{v}_{z,+}$ plane are directly related to the energy flux as described in Eq. (40) and provide fundamental information about the properties of the energy flux. Figure 11(a) reveals that $\Gamma(\hat{\sigma}_{zz}, \hat{v}_{z,+})$ exhibits a higher density of states in the negative stress range, which is referred to as the "stress band" in this paper. A high density of states is observed inside the stress band, and it

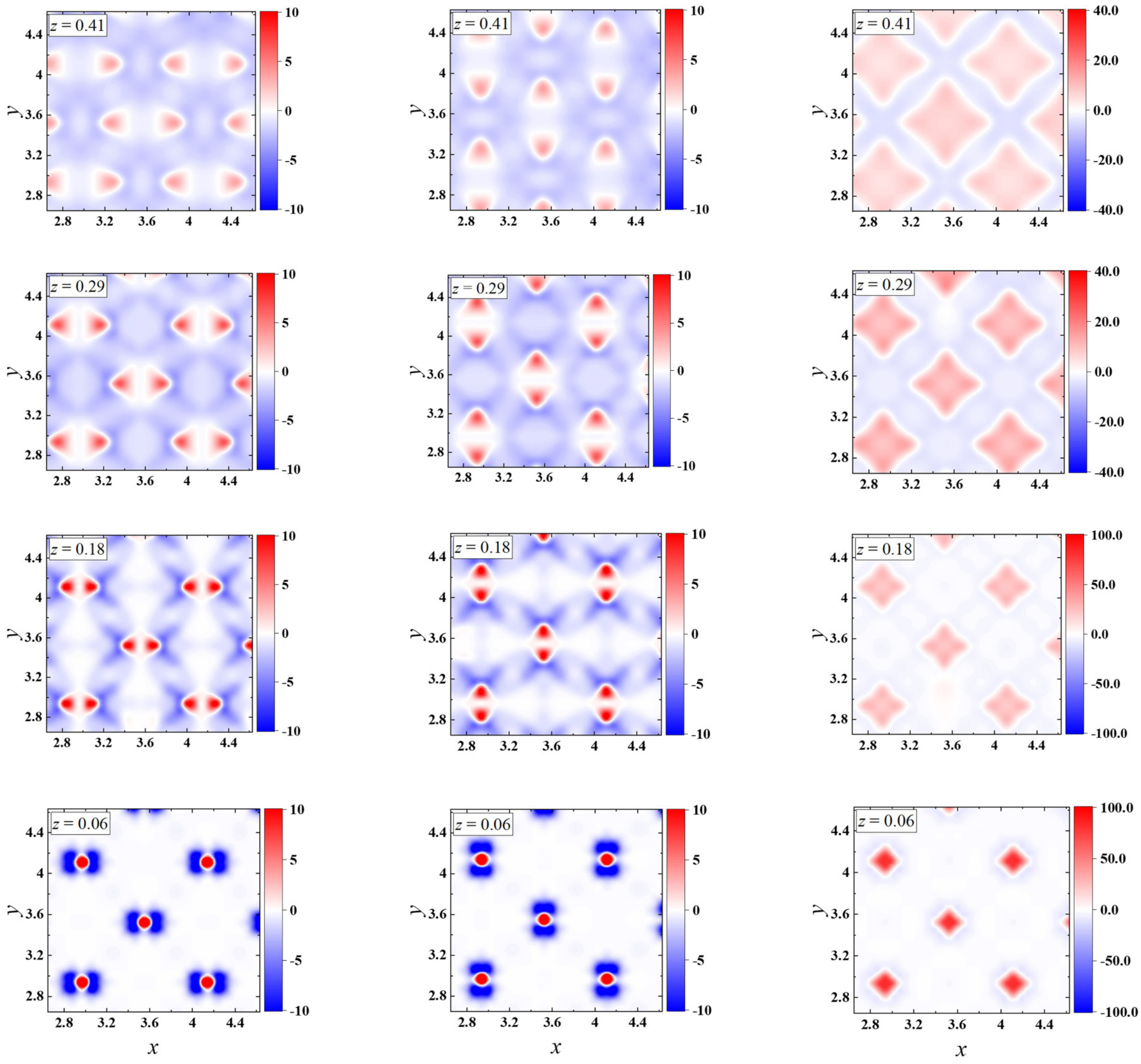

(a) $< P_{xx} >$ (b) $< P_{yy} >$ (c) $< P_{zz} >$

FIG. 6. Three-dimensional stress at the solid-liquid interface for $\varepsilon_{fs} = 0.5$. Panels (a)–(c) present the xx, yy, and zz component of the stress, namely, $\langle P_{xx} \rangle$, $\langle P_{yy} \rangle$, and $\langle P_{zz} \rangle$, respectively, which are calculated at $z = 0.06$, 0.18, 0.29, and 0.41 between the contacting solid and liquid layers.

decays in the positive stress direction outside the band. This band property allows for a better understanding of the field quantities determined from single-interaction-based physical quantities. The energy flux result in Fig. 11(b) is reasonable, where the signs (positive or negative) of $\hat{\sigma}_{zz}$ and $\hat{v}_{z,+}$ determine the sign of the energy flux. Figures 11(b) and 11(d) present the energy flux density distribution, which is dependent on the single-interaction-based stress $\hat{\sigma}_{zz}$, where the regions with positive and negative values are detected inside and outside the stress band. This single-interaction-based stress $\hat{\sigma}_{zz}$ can be understood based on the distance between the solid atom and liquid molecule $\hat{r}_{sl}$, as expressed by $\Gamma_{\hat{r}_{sl}}(\hat{\sigma}_{zz})/\Gamma(\hat{\sigma}_{zz})$ in Fig. 12. An intrinsic property of the intermolecular force reveals that the energy transfers inside and outside the stress bands correspond to the influences of the stress at long and short intermolecular distances, respectively. More fundamental mechanisms are discussed in the following section. Notably, an insightful result based on the intermolecular distance was reported by Ohara [33,34], who conducted a study focusing on the energy transfer rate between molecules in the liquid and between solid atoms and liquid molecules at a solid-liquid interface. Ohara presented a relationship between the molecular structure in the liquid (radial distribution function) and the instantaneous energy transport, which is dependent on the distance between the molecules.

Figure 13(a) presents the time-averaged density distribution $\Gamma(\hat{\sigma}_{zz}) = \langle \int_{-\infty}^{\infty} \Gamma^{(t)}(\hat{\sigma}_{zz}, \hat{v}_{z,+})\, d\hat{v}_{z,+} \rangle$ and energy flux density distribution $\Gamma_{\hat{j}_z}(\hat{\sigma}_{zz}) = \langle \int_{-\infty}^{\infty} \hat{j}_z \Gamma^{(t)}(\hat{\sigma}_{zz}, \hat{v}_{z,+})\, d\hat{v}_{z,+} \rangle$ as functions of the single-interaction-based stress $\hat{\sigma}_{zz}$ for $\varepsilon_{fs} =$ 0.5, 1.0, 1.5, and 2.0. With respect to the result outside the stress band ($\hat{\sigma}_{zz} > 0$), $\Gamma(\hat{\sigma}_{zz})$ decays exponentially in the positive $\hat{\sigma}_{zz}$ direction, and there are critical $\Gamma_{\hat{j}_z}(\hat{\sigma}_{zz})$ values that represent the maximum and minimum values ($\hat{\sigma}_{zz} > 0$). The value of $\hat{\sigma}_{zz}$ corresponding to the critical maximum $\Gamma_{\hat{j}_z}(\hat{\sigma}_{zz})$

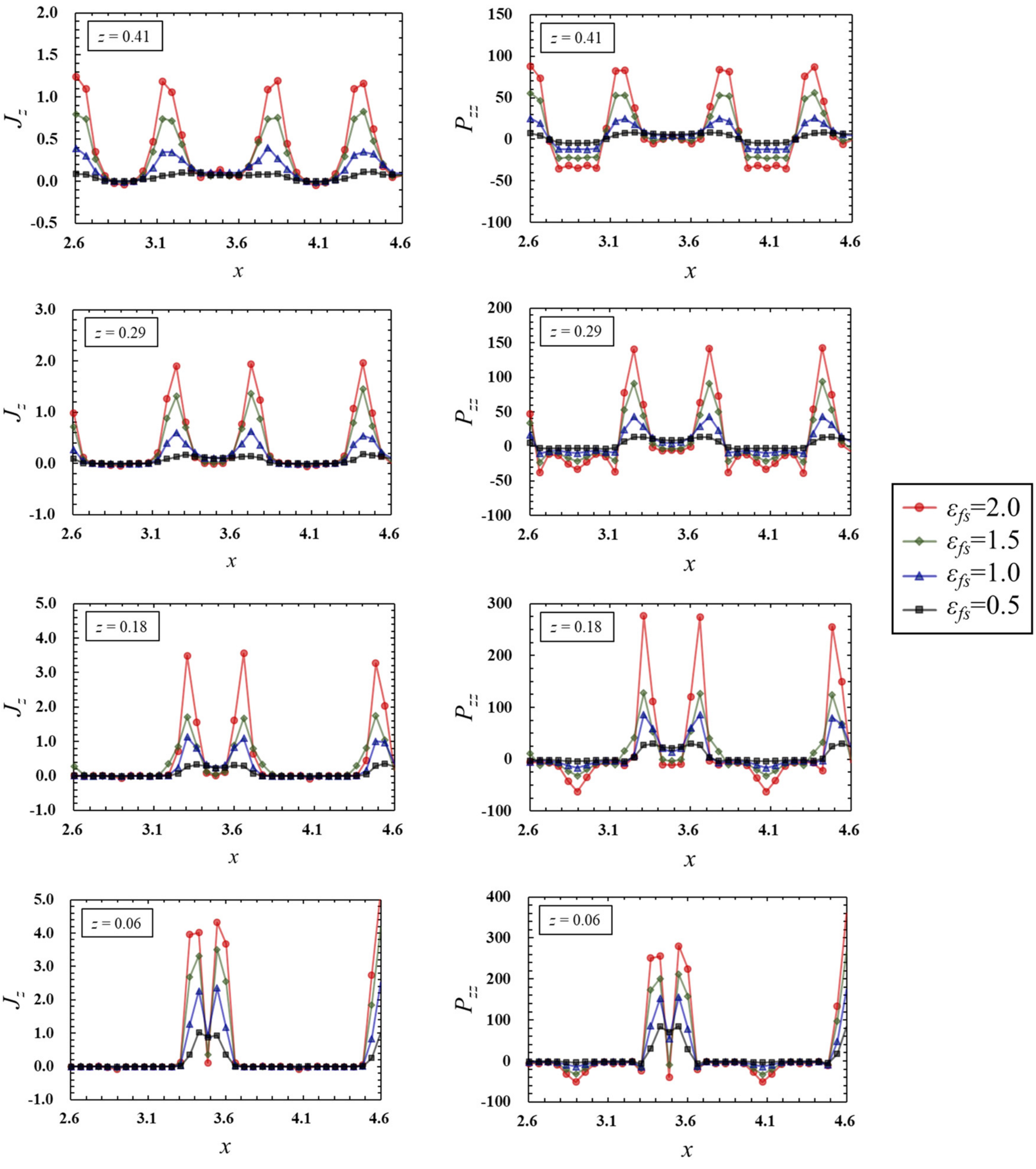

(a) (b)

FIG. 7. (a) The z component of the local heat flux and (b) zz component of the stress along the x axis for $\varepsilon_{fs} = 0.5$, 1.0, 1.5, and 2.0. The heat fluxes and stresses at $y = 3.5$ are calculated at $z = 0.06$, 0.18, 0.29, and 0.41 for all the cases.

is the most dominant intermolecular stress at the single-interaction level and contributes to the macroscopic energy flux J_z. Several negative energy fluxes are observed inside the stress band ($\hat{\sigma}_{zz}<0$); however, the integration of $\Gamma_{\hat{j}_z}(\hat{\sigma}_{zz})$ over $\hat{\sigma}_{zz}$ reveals that the predominant contribution of $\hat{\sigma}_{zz}$ to the macroscopic heat flux is around the critical $\Gamma_{\hat{j}_z}$ value. The critical $\Gamma_{\hat{j}_z}(\hat{\sigma}_{zz})$ shifts in the positive $\hat{\sigma}_{zz}$ direction, and the corresponding energy flux is enhanced with an increase in ε_{fs}. The positive and negative values of $\Gamma_{\hat{j}_z}(\hat{\sigma}_{zz})$ correspond to the regions detected at $\hat{\sigma}_{zz} > 0$, as shown in Fig. 11(d). An enlarged image is shown in Fig. 13(b). In the stress band ($\hat{\sigma}_{zz}<0$), a higher value of $\Gamma(\hat{\sigma}_{zz})$ is observed when compared with the outside of the band, and the peak value is within the immediate vicinity of $\hat{\sigma}_{zz} = 0$. The peak value reflects the intermolecular force when the particles are interacting under the condition wherein the distance between the particles is relatively long. As predicted, the peak value in the stress band structure is dependent on the cutoff distance, as discussed in Appendix A. The energy flux inside the band exhibits a negative value due to the high density of states in the negative stress region. The mechanism is detailed in the next section.

Figure 14 presents the time-averaged energy flux density distribution per single interaction $\Gamma_{\hat{j}_\alpha}(\hat{\sigma}_{zz})/\Gamma(\hat{\sigma}_{zz})$ under the single-interaction-based stress $\hat{\sigma}_{zz}$. The value outside the stress band indicates that the energy flux per single interaction is higher when ε_{fs} is low. In particular, the influence of the

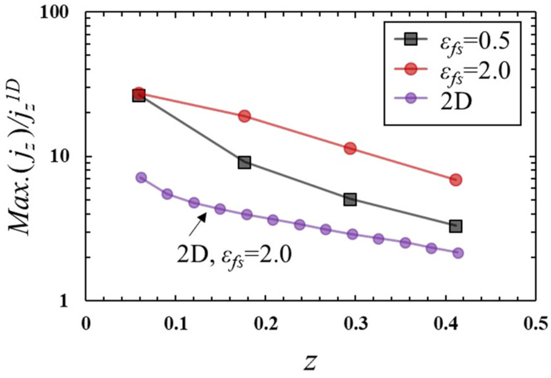

FIG. 8. Properties of the 3D heat flux between the contacting solid-liquid layers; the 2D heat flux at $x = 3.55$ from Fig. 2(a) is included for comparison. The maximum values of the 3D heat flux at each z axis are adopted, and the results are normalized using the 1D heat flux j_z^{1D} for each case of ε_{fs}.

solid-liquid strength based on the single-interaction level can be described as follows. The high interaction strength allows for the density of states outside the band to be high, which leads to a high energy flux outside the band. This contributes predominantly to the macroscopic energy flux. For the low interaction strength, the energy flux per single interaction is higher, as shown in Fig. 14. However, it does not fully compensate for the macroscopic heat flux owing to the low density of states outside the band.

TABLE I. Ratio of local heat flux to local stress, $\langle J_z\rangle/\langle P_{zz}\rangle$, in the contacting solid and liquid layers for various wetting parameters of ε_{fs}. The values are obtained in the same manner as the results presented in Fig. 9.

	z			
ε_{fs}	0.06	0.18	0.29	0.41
0.5	0.0116	0.0104	0.0096	0.0090
1.0	0.0146	0.0123	0.0123	0.0119
1.5	0.0157	0.0126	0.0136	0.0125
2.0	0.0147	0.0122	0.0132	0.0118

To clarify the results in Fig. 11 based on the 1D distribution, Fig. 15 presents the time-averaged density-of-states distribution $\Gamma(\hat{v}_+) = \langle\int_{-\infty}^{\infty}\Gamma^{(t)}(\hat{\sigma}_{zz}, \hat{v}_{z,+})\,d\hat{\sigma}_{zz}\rangle$ and energy flux density distribution $\Gamma_{\hat{j}_z}(\hat{v}_+) = \langle\int_{-\infty}^{\infty}\hat{j}_z\Gamma^{(t)}(\hat{\sigma}_{zz}, \hat{v}_{z,+})\,d\hat{\sigma}_{zz}\rangle$ for $\varepsilon_{fs} = 0.5$, 1.0, 1.5, and 2.0. The results are obtained for the entire (inside and outside) region [Fig. 15(a)], inside region [Fig. 15(b)], and outside region [Fig. 15(c)] of the stress band. Based on the results, $\Gamma(\hat{v}_{z,+})$ inside the band is predominant. Moreover, the orders of $\Gamma_{\hat{j}_z}(\hat{v}_{z,+})$ inside and outside the band are almost the same. The result for the entire region [Fig. 15(a)] reveals that $\Gamma_{\hat{j}_z}(\hat{v}_{z,+})$ is less than a tenth of the value inside and outside the band. Figure 16 presents the time-averaged energy flux rate per single interaction $\Gamma_{\hat{j}_z}(\hat{v}_{z,+})/\Gamma(\hat{v}_{z,+})$ for the entire region [Fig. 16(a)], inside region [Fig. 16(b)], and outside region [Fig. 16(c)] of the stress band. The profiles inside and outside the band exhibit

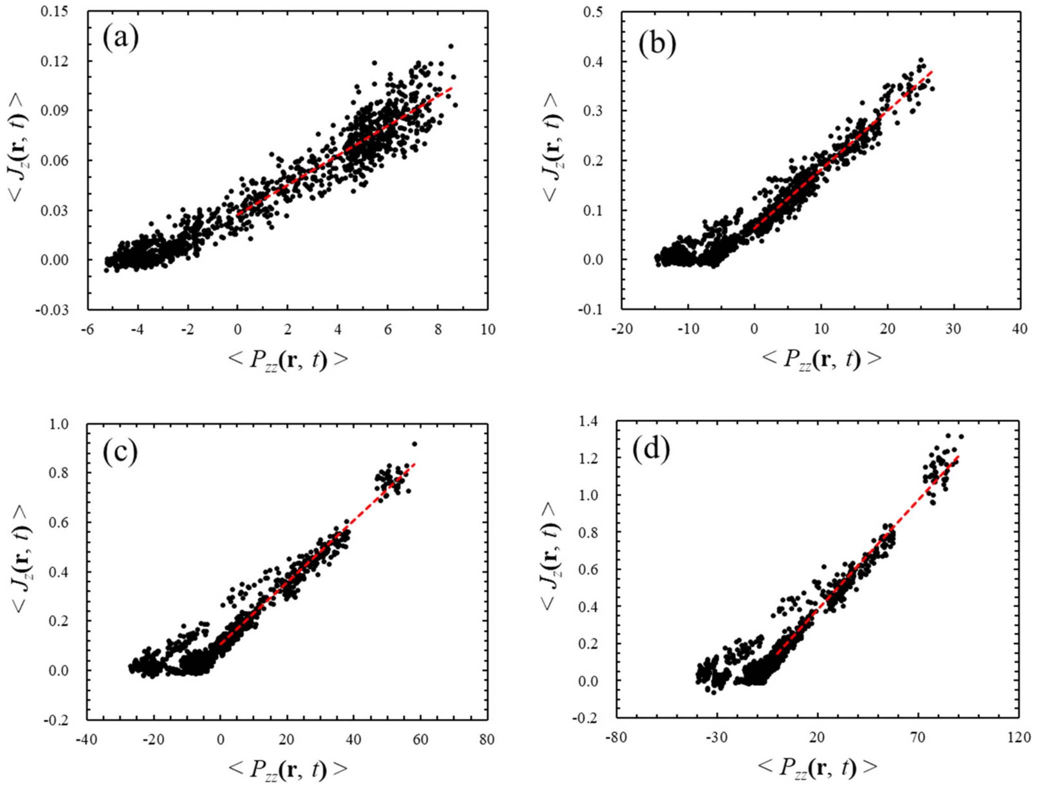

FIG. 9. Relationship between the local heat flux and local stress at $z = 0.41$, for ε_{fs} = (a) 0.5, (b) 1.0, (c) 1.5, and (d) 2.0. The red line indicates the linear fitted line at $\langle P_{zz}(\mathbf{r}, t)\rangle$>0.

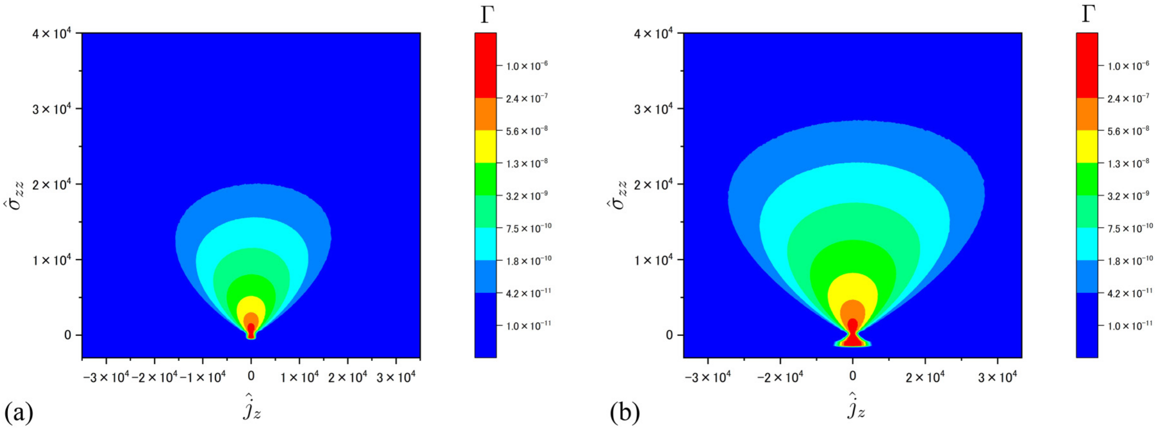

FIG. 10. Time-averaged density-of-states distribution $\Gamma(\hat{\sigma}_{zz}, \hat{j}_z) = \langle \Gamma^{(t)}(\hat{\sigma}_{zz}, \hat{j}_z)\rangle$ in the plane of the single-interaction-based stress $\hat{\sigma}_{zz}$ and energy-flux $\hat{j}_z$, where each value is calculated within an area of $d\hat{\sigma}_{zz} \times d\hat{j}_z = 5.2 \times 10^2 \times 2.7 \times 10^2$, and 5.0×10^9 time steps are considered for the time average. The results are presented for the cases of $\varepsilon_{fs} =$ (a) 0.5 and (b) 2.0.

linear relationships between $\Gamma_{\hat{j}_z}(\hat{v}_{z,+})/\Gamma(\hat{v}_{z,+})$ and $\hat{v}_{z,+}$. Outside the band, the energy flux rate $\Gamma_{\hat{j}_z}(\hat{v}_{z,+})/\Gamma(\hat{v}_{z,+})$ is high and exhibits a positive gradient in the positive $\hat{v}_{z,+}$ direction due to the positive stress value. Moreover, the energy flux rate inside the band is low and exhibits a negative gradient due to the negative stress value. As a result of the sum of the values

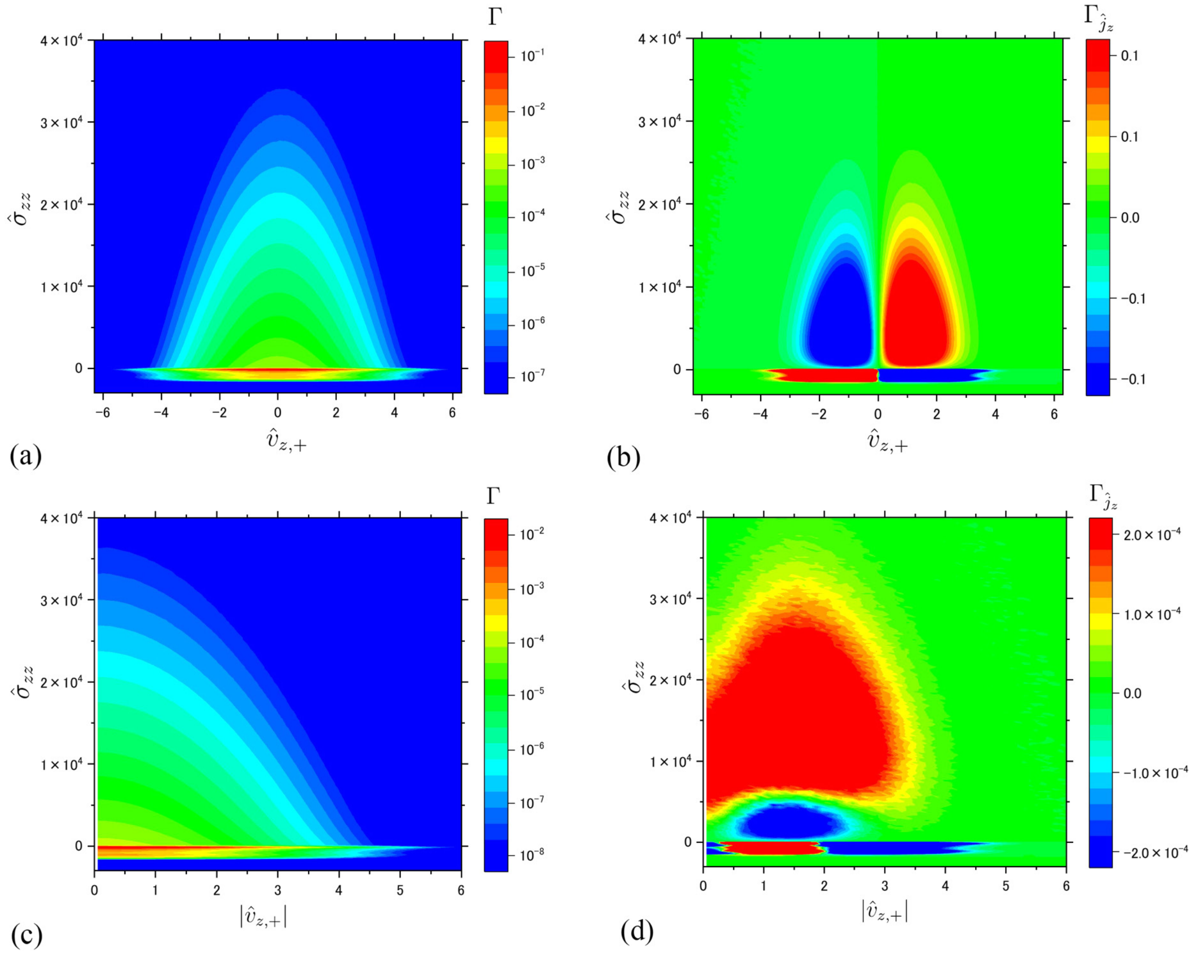

FIG. 11. (a) Time-averaged density distribution $\Gamma(\hat{\sigma}_{zz}, \hat{v}_{z,+}) = \langle \Gamma^{(t)}(\hat{\sigma}_{zz}, \hat{v}_{z,+})\rangle$ and (b) energy flux density distribution $\Gamma_{\hat{j}_z}(\hat{\sigma}_{zz}, \hat{v}_{z,+}) = \langle \hat{j}_z \Gamma^{(t)}(\hat{\sigma}_{zz}, \hat{v}_{z,+})\rangle$ in the plane of the single-interaction-based stress $\hat{\sigma}_{zz}$ and velocity $\hat{v}_{z,+} = \hat{v}_{z,s} + \hat{v}_{z,l}$ for $\varepsilon_{fs} = 2.0$. Each value is calculated within an area of $d\hat{\sigma}_{zz} \times d\hat{v}_{z,+} = 2.3 \times 10^2 \times 1.0 \times 10^{-1}$, and 5.0×10^9 time steps are considered for the time average. The results of $\Gamma(\hat{\sigma}_{zz}, \hat{v}_{z,+})$ and $\Gamma_{\hat{j}_z}(\hat{\sigma}_{zz}, \hat{v}_{z,+})$ in the $\hat{\sigma}_{zz}$-$|\hat{v}_{z,+}|$ plane are presented in (c) and (d), respectively.

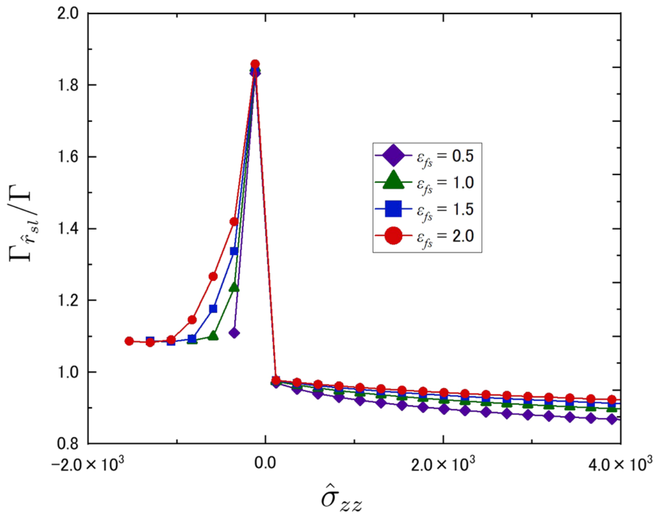

FIG. 12. Distance between the solid atom and liquid molecule in the z component of the single-interaction-based stress $\hat{\sigma}_{zz}$ for $\varepsilon_{fs} = 0.5$, 1.0, 1.5, and 2.0. The time-averaged density-of-states distribution $\Gamma(\hat{\sigma}_{zz}) = \langle\int_{-\infty}^{\infty}\Gamma^{(t)}(\hat{\sigma}_{zz}, \hat{v}_{z,+})\,d\hat{v}_{z,+}\rangle$ and the distance density distribution $\Gamma_{\hat{r}_{sl}}(\hat{\sigma}_{zz}) = \langle\int_{-\infty}^{\infty}\hat{r}_{sl}\Gamma^{(t)}(\hat{\sigma}_{zz}, \hat{v}_{z,+})\,d\hat{v}_{z,+}\rangle$ are calculated and expressed in terms of the ratio $\Gamma_{\hat{r}_{sl}}(\hat{\sigma}_{zz})/\Gamma(\hat{\sigma}_{zz})$.

inside and outside the band, the result presented in Fig. 16(a) is obtained.

Figure 17 presents the time-averaged density distribution $\Gamma(\hat{j}_z) = \langle\int_{-\infty}^{\infty}\Gamma^{(t)}(\hat{\sigma}_{zz}, \hat{j}_z)\,d\hat{\sigma}_{zz}\rangle$ and stress density distribution $\Gamma_{\hat{\sigma}_{zz}}(\hat{j}_z) = \langle\int_{-\infty}^{\infty}\hat{\sigma}_{zz}\Gamma^{(t)}(\hat{\sigma}_{zz}, \hat{j}_z)\,d\hat{\sigma}_{zz}\rangle$ in the single-interaction-based energy flux $\hat{j}_z$ for $\varepsilon_{fs} = 0.5$, 1.0, 1.5, and 2.0. The result in Fig. 17(a), which is obtained from the entire stress range (inside and outside of the stress band), reveals that the contribution of $\hat{j}_z$ to $\Gamma_{\hat{\sigma}_{zz}}(\hat{j}_z)$ is significant around $\hat{j}_{zz} = 0$. Moreover, $\Gamma_{\hat{\sigma}_{zz}}(\hat{j}_z)$ exhibits positive and negative values in the immediate vicinity of $\hat{j}_z = 0$, although the values become positive along the positive and negative $\hat{j}_z$ directions and decay to zero. The results for the inside [Fig. 17(b)] and outside regions of the stress band [Fig. 17(c)] are necessary for understanding $\Gamma_{\hat{\sigma}_{zz}}(\hat{j}_z)$ in Fig. 17(a). Inside the stress band, the density of states is found within the narrow ranges of $\hat{j}_z$, with the highest value at $\hat{j}_z = 0$, where the stress density distribution $\Gamma_{\hat{\sigma}_{zz}}(\hat{j}_z)$ exhibits a high negative value that is satisfactory inside the band. On the other hand, $\Gamma(\hat{j}_z)$ outside the band [Fig. 17(c)] occupies a wide range of $\hat{j}_z$, with the highest value at $\hat{j}_z = 0$, where $\Gamma_{\hat{\sigma}_{zz}}(\hat{j}_z)$ shows high values in the wide range of $\hat{j}_z$. Due to these properties, $\Gamma_{\hat{\sigma}_{zz}}(\hat{j}_z)$ exhibits two critical values in the positive and negative $\hat{j}_z$ directions [see Fig. 17(a)].

Thus, the macroscopic transport quantities of the heat flux and stress across a solid-liquid interface are related to the 2D density distribution of the single-interaction-based stress and energy flux $\Gamma(\hat{\sigma}_{zz}, \hat{j}_z)$ (Fig. 10), and the 1D density distributions of $\Gamma(\hat{\sigma}_{zz})$ (Fig. 13) and $\Gamma(\hat{j}_z)$ (Fig. 17).

The results for the single-interaction-based energy flux at the subatomic scale are presented in Fig. 18 as the [Fig. 18(a)] time-averaged density distribution $\Gamma^{(\mathbf{r}_1)}(\hat{\sigma}_{zz}, \hat{v}_{z,+}) = \langle\Gamma^{(\mathbf{r}_1,t)}(\hat{\sigma}_{zz}, \hat{v}_{z,+})\rangle$ and [Fig. 18(b)] energy flux density distribution $\Gamma^{(\mathbf{r}_1)}_{\hat{j}_z}(\hat{\sigma}_{zz}, \hat{v}_{z,+}) = \langle\hat{j}_z\Gamma^{(\mathbf{r}_1,t)}(\hat{\sigma}_{zz}, \hat{v}_{z,+})\rangle$ in the

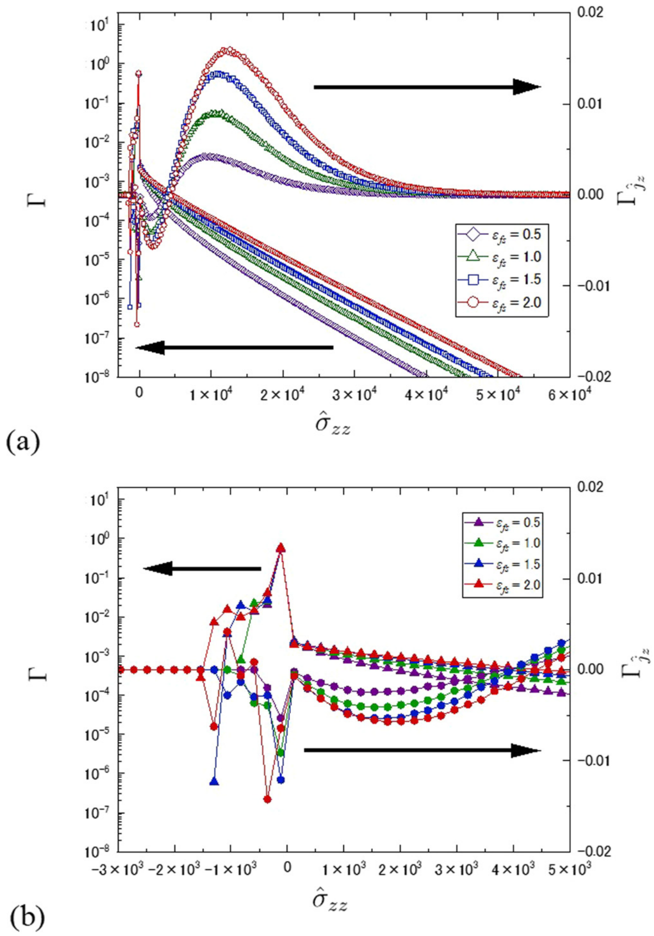

FIG. 13. (a) Time-averaged density-of-states distribution $\Gamma(\hat{\sigma}_{zz}) = \langle\int_{-\infty}^{\infty}\Gamma^{(t)}(\hat{\sigma}_{zz}, \hat{v}_{z,+})\,d\hat{v}_{z,+}\rangle$ and energy flux density distribution $\Gamma_{\hat{j}_z}(\hat{\sigma}_{zz}) = \langle\int_{-\infty}^{\infty}\hat{j}_z\Gamma^{(t)}(\hat{\sigma}_{zz}, \hat{v}_{z,+})\,d\hat{v}_{z,+}\rangle$ in the single-interaction-based stress $\hat{\sigma}_{zz}$ for $\varepsilon_{fs} = 0.5$, 1.0, 1.5, and 2.0. (b) Enlarged view of the stress band region.

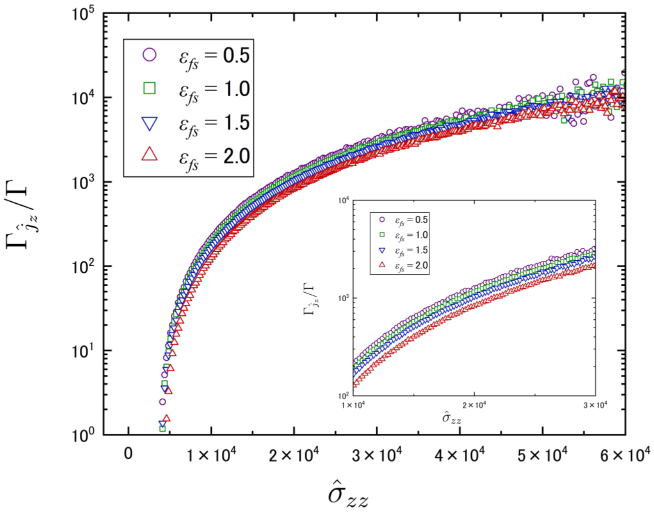

FIG. 14. Time-averaged energy flux density distribution per single interaction $\Gamma_{\hat{j}_z}(\hat{\sigma}_{zz})/\Gamma(\hat{\sigma}_{zz})$ in the single-interaction-based stress $\hat{\sigma}_{zz}$ with an enlarged view.

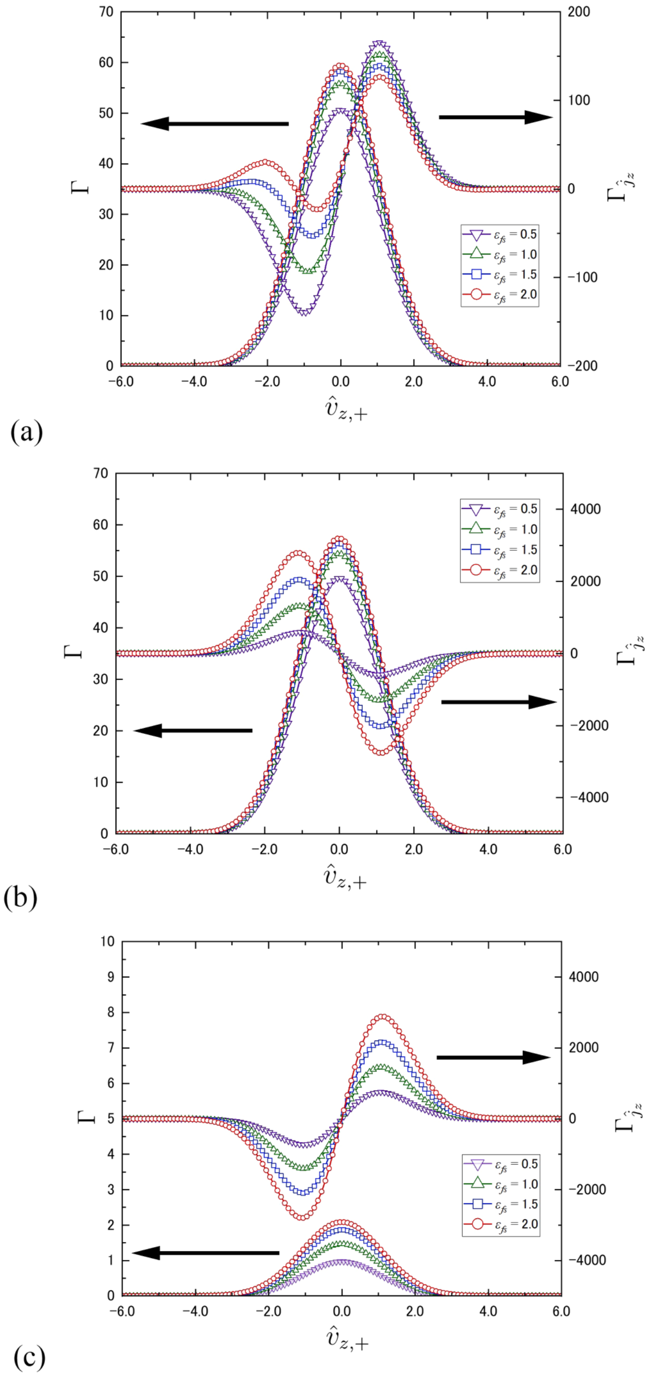

FIG. 15. Time-averaged density-of-states distribution $\Gamma(\hat{v}_{z,+}) = \langle \int_{-\infty}^{\infty} \Gamma^{(t)}(\hat{\sigma}_{zz}, \hat{v}_{z,+})\, d\hat{\sigma}_{zz} \rangle$ and energy flux density distribution $\Gamma_{\hat{j}_z}(\hat{v}_{z,+}) = \langle \int_{-\infty}^{\infty} \hat{j}_z \Gamma^{(t)}(\hat{\sigma}_{zz}, \hat{v}_{z,+})\, d\hat{\sigma}_{zz} \rangle$ for $\varepsilon_{fs} = 0.5$, 1.0, 1.5, and 2.0, where $\hat{v}_{z,+}$ is defined as $\hat{v}_{z,+} = \hat{v}_{z,s} + \hat{v}_{z,l}$ for (a) entire (inside and outside) region, (b) inside region, and (c) outside region, of the stress band.

plane of the single-interaction-based stress $\hat{\sigma}_{zz}$ and velocity $\hat{v}_{z,+} = (\hat{v}_{z,s} + \hat{v}_{z,l})$. The results are calculated at $\mathbf{r_1} = (3.8, 3.5, 0.41)$ within an area of $dx \times dy = 0.059 \times 0.059$, where a strong heat flux is detected, as shown in Fig. 3(c). The comparison between the results in Figs. 11 and 18 reveals that the strong heat flux detected at the subatomic scale exhibits a similar trend for the overall interfacial thermal transport, thus suggesting that it is the source of the interfacial thermal transport. Figure 19(a) presents the time-averaged density distribution $\Gamma^{(\mathbf{r}_1)}(\hat{\sigma}_{zz}) = \langle \int_{-\infty}^{\infty} \Gamma^{(\mathbf{r}_1,t)}(\hat{\sigma}_{zz}, \hat{v}_{z,+})\, d\hat{v}_{z,+} \rangle$

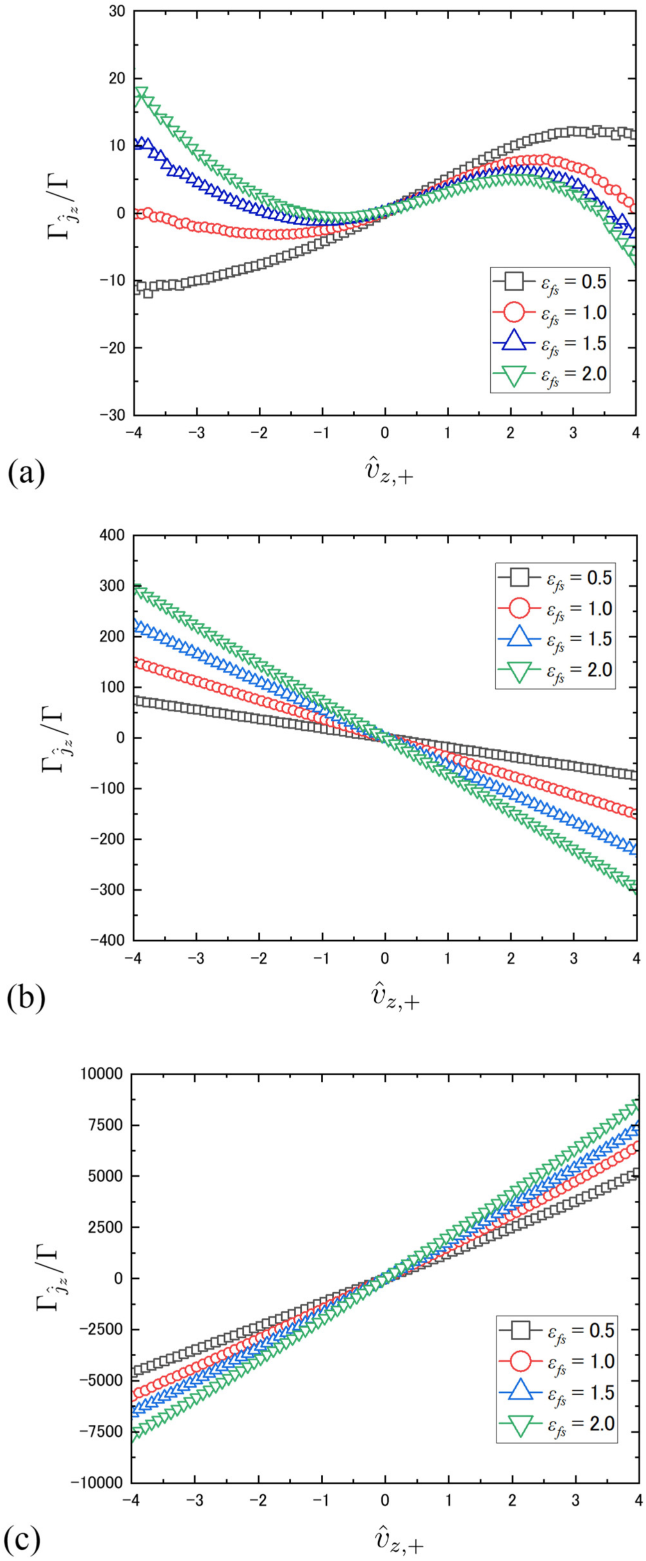

FIG. 16. Time-averaged energy flux density distribution per single-interaction $\Gamma_{\hat{j}_z}(\hat{v}_{z,+})/\Gamma(\hat{v}_{z,+})$ for (a) entire (inside and outside) region, (b) inside region, and (c) outside region, of the stress band.

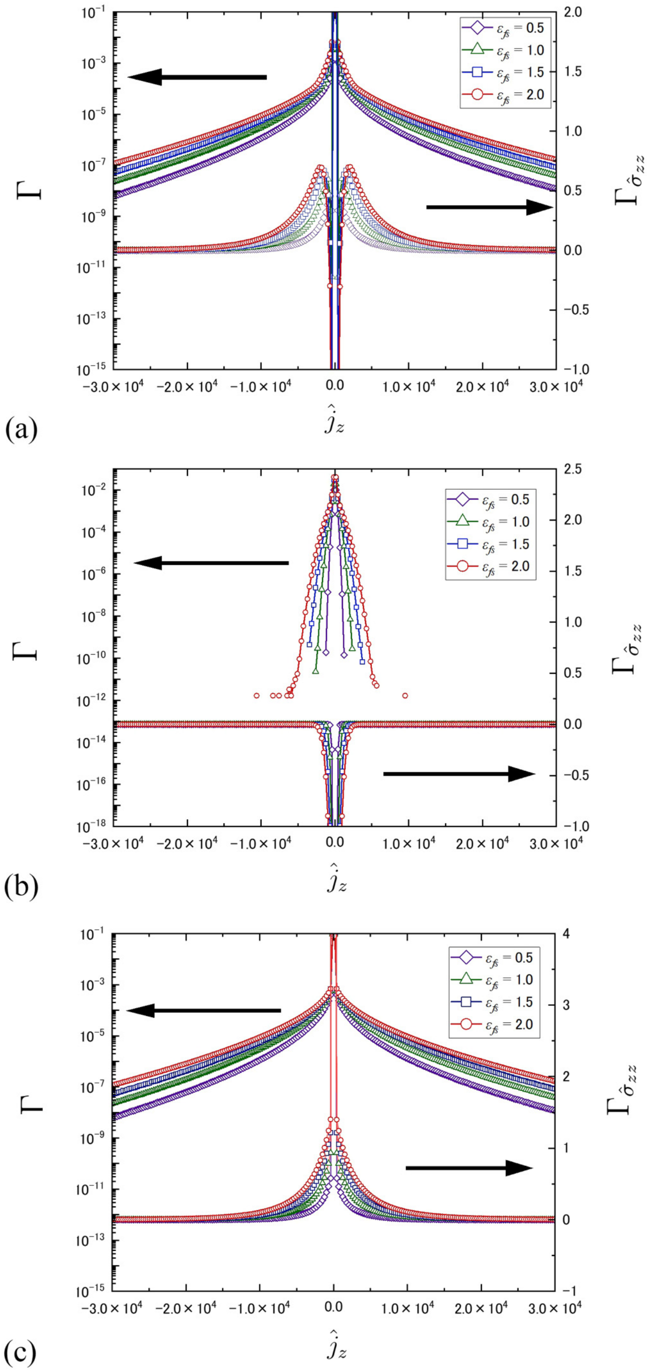

FIG. 17. Time-averaged density distribution $\Gamma(\hat{j}_z) = \langle\int_{-\infty}^{\infty}\Gamma^{(t)}(\hat{\sigma}_{zz}, \hat{j}_z)\,d\hat{\sigma}_{zz}\rangle$ and stress density distribution $\Gamma_{\hat{\sigma}_{zz}}(\hat{j}_z) = \langle\int_{-\infty}^{\infty}\hat{\sigma}_{zz}\Gamma^{(t)}(\hat{\sigma}_{zz}, \hat{j}_z)\,d\hat{\sigma}_{zz}\rangle$ for $\varepsilon_{fs} = 0.5$, 1.0, 1.5, and 2.0. The results are presented for (a) entire region, (b) inside the band, and (c) outside the band.

and energy flux density distribution $\Gamma^{(\mathbf{r}_1)}_{\hat{j}_z}(\hat{\sigma}_{zz}) = \langle\int_{-\infty}^{\infty}\hat{j}_z\Gamma^{(\mathbf{r}_1,t)}(\hat{\sigma}_{zz}, \hat{v}_{z,+})\,d\hat{v}_{z,+}\rangle$ for $\varepsilon_{fs} = 0.5, 1.0, 1.5$, and 2.0. Figure 19(b) presents an enlarged view of the stress band. The comparison of Figs. 13 and 19 reveals that the macroscopic energy transfer reflected the energy flux at the subatomic scale, where the strong energy flux is detected.

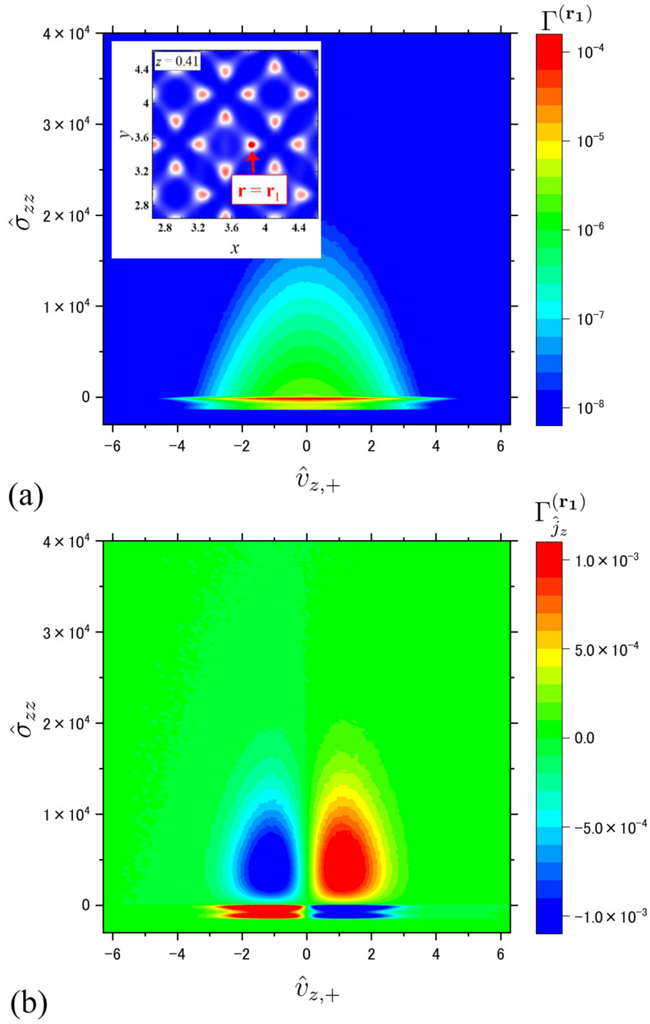

FIG. 18. (a) Time-averaged density distribution $\Gamma^{(\mathbf{r}_1)}(\hat{\sigma}_{zz}, \hat{v}_{z,+}) = \langle\Gamma^{(\mathbf{r}_1,t)}(\hat{\sigma}_{zz}, \hat{v}_{z,+})\rangle$ and (b) energy flux density distribution $\Gamma^{(\mathbf{r}_1)}_{\hat{j}_z}(\hat{\sigma}_{zz}, \hat{v}_{z,+}) = \langle\hat{j}_z\Gamma^{(\mathbf{r}_1,t)}(\hat{\sigma}_{zz}, \hat{v}_{z,+})\rangle$ in the plane of the single-interaction-based stress $\hat{\sigma}_{zz}$ and velocity $\hat{v}_{z,+} = (\hat{v}_{z,s} + \hat{v}_{z,l})$. Each value is calculated in the area of $d\hat{\sigma}_{zz} \times d\hat{v}_{z,+} = 2.3 \times 10^2 \times 1.0 \times 10^{-1}$, and 5×10^9 time steps are considered for the time average. The values are obtained at $\mathbf{r}_1 = (3.8, 3.5, 0.41)$ with the area of $dx \times dy = 0.059 \times 0.059$. The position $\mathbf{r}_1$ is represented for the result of the heat flux distribution at $z = 0.41$, as shown in Fig. 3(c).

Thereafter, we focus on $\mathbf{r_2} = (4.1, 3.5, 0.41)$, where the strong energy flux is not detected, as shown in Fig. 3(c). The 2D results of $\Gamma^{(\mathbf{r}_2)}(\hat{\sigma}_{zz}, \hat{v}_{z,+})$ and $\Gamma^{(\mathbf{r}_2)}_{\hat{j}_z}(\hat{\sigma}_{zz}, \hat{v}_{z,+})$ are shown in Fig. 20, whereas $\Gamma^{(\mathbf{r}_2)}(\hat{\sigma}_{zz})$ and $\Gamma^{(\mathbf{r}_2)}_{\hat{j}_z}(\hat{\sigma}_{zz})$ are shown in Fig. 21. As shown in Fig. 20, the density of states and the corresponding energy flux density at $\mathbf{r_2}$ are lower than those in Fig. 18. The energy flux density for the single-interaction-based stress $\hat{\sigma}_{zz}$ shown in Fig. 21 reveals that the energy transfer in the stress band is dominant at $\mathbf{r_2}$; $\Gamma^{(\mathbf{r}_2)}_{\hat{j}_z}(\hat{\sigma}_{zz}) \approx 0$ at $\hat{\sigma}_{zz} > 0$. This is the cause of the negative stress and heat flux at the subatomic scale, as shown in Fig. 9.

In Sec. V the linear relationship between the stress and heat flux at the subatomic scale is presented. In this section,

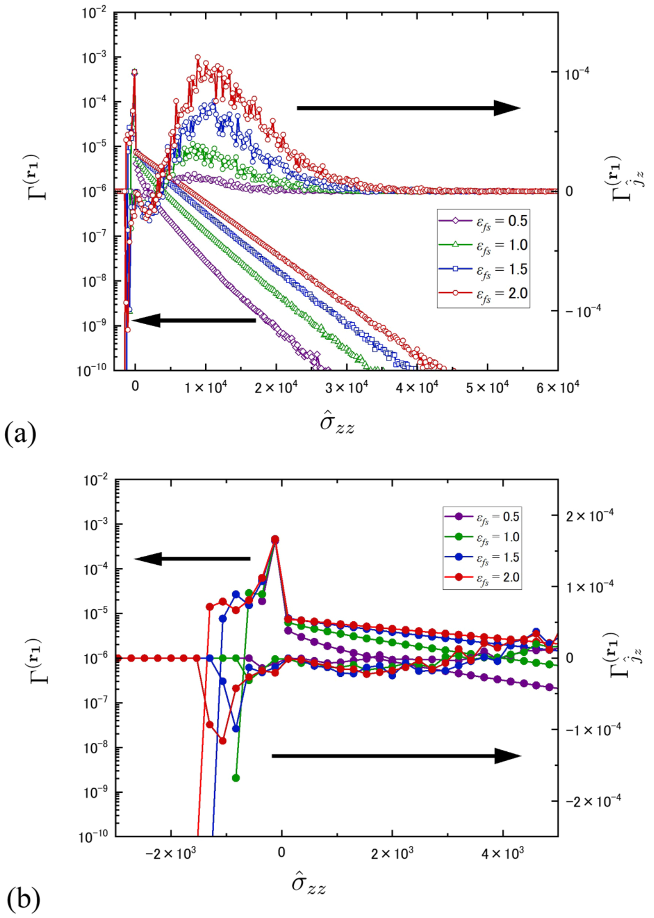

FIG. 19. (a) Time-averaged density distribution $\Gamma^{(\mathbf{r}_1)}(\hat{\sigma}_{zz}) = \langle \int_{-\infty}^{\infty} \Gamma^{(\mathbf{r}_1,t)}(\hat{\sigma}_{zz}, \hat{v}_{z,+})\, d\hat{v}_{z,+} \rangle$ and energy flux density distribution $\Gamma^{\mathbf{r}_1}_{\hat{j}_z}(\hat{\sigma}_{zz}) = \langle \int_{-\infty}^{\infty} \hat{j}_z \Gamma^{(\mathbf{r}_1,t)}(\hat{\sigma}_{zz}, \hat{v}_{z,+})\, d\hat{v}_{z,+} \rangle$ for $\varepsilon_{fs} = 0.5, 1.0, 1.5$, and 2.0. (b) Enlarged view of the stress band. The values are obtained at $\mathbf{r}_1 = (3.8, 3.5, 0.41)$.

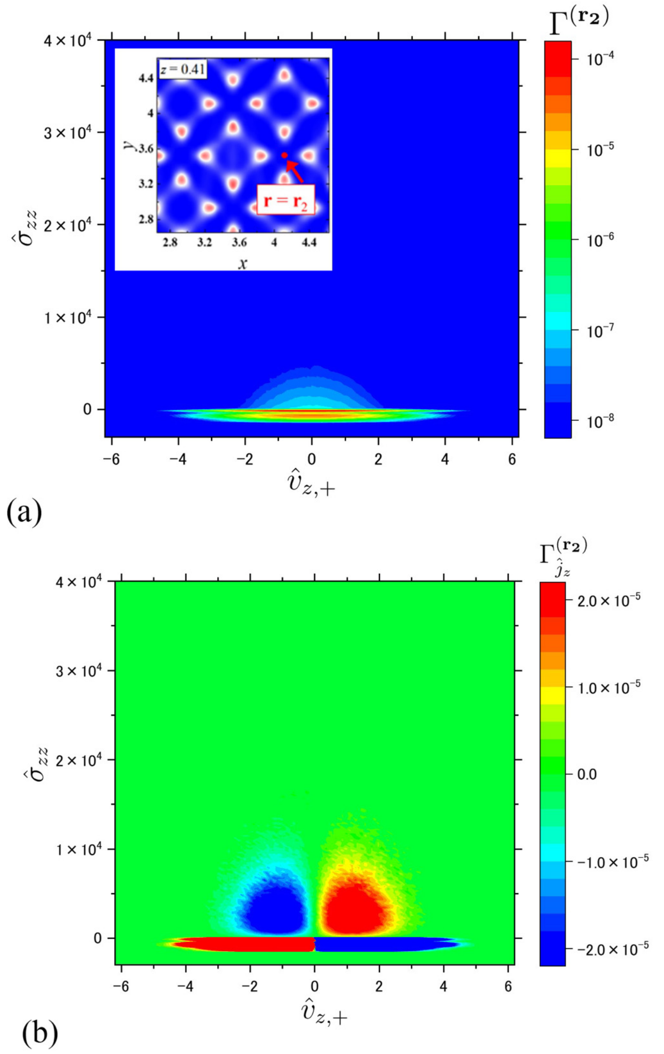

FIG. 20. (a) Time-averaged density distribution $\Gamma^{(\mathbf{r}_2)}(\hat{\sigma}_{zz}, \hat{v}_{z,+}) = \langle \Gamma^{(\mathbf{r}_2,t)}(\hat{\sigma}_{zz}, \hat{v}_{z,+}) \rangle$ and (b) energy flux density distribution $\Gamma^{(\mathbf{r}_2)}_{\hat{j}_z}(\hat{\sigma}_{zz}, \hat{v}_{z,+}) = \langle \hat{j}_z \Gamma^{(\mathbf{r}_2,t)}(\hat{\sigma}_{zz}, \hat{v}_{z,+}) \rangle$ in the plane of the single-interaction-based stress $\hat{\sigma}_{zz}$ and velocity $\hat{v}_{z,+} = (\hat{v}_{z,s} + \hat{v}_{z,l})$, where each value is calculated in the area of $d\hat{\sigma}_{zz} \times d\hat{v}_{z,+} = 2.3 \times 10^2 \times 1.0 \times 10^{-1}$, and 5×10^9 time steps are considered for the time average. The values are obtained at $\mathbf{r_2} = (4.1, 3.5, 0.41)$ with the area of $dx \times dy = 0.059 \times 0.059$. The position $\mathbf{r}_2$ is represented for the result of the heat flux distribution at $z = 0.41$, as shown in Fig. 3(c).

the transport quantities of the stress and heat flux at the macroscopic and subatomic scales are related to the single-interaction-based stress and energy flux. The properties of the single-interaction-based energy flux at the macroscopic and subatomic scales indicate that the thermal transport property at the macroscopic scale can be explained by the single-interaction-based energy flux at the subatomic scale, where a strong heat flux is detected as a time-averaged value.

VII. THERMAL TRANSPORT MECHANISM BASED ON SINGLE-INTERACTION-BASED STRESS AND ENERGY FLUX

In the previous section, the macroscopic thermal transport property at the interface is associated with the time-averaged energy flux at the subatomic scale using the single-interaction-based energy flux. The results indicate that the density states of the field transport quantities have a "stress band" in the plane of the single-interaction-based stress and other variables. The energy flux is composed of the positive and negative energy fluxes inside and outside the band, which contribute specifically to the net energy flux. The contribution outside the band to the net energy flux is dominant. This section details the mechanism of the positive and negative energy transport inside and outside the stress bands by the density distribution using the variables related to the physical quantities of the atom or molecule, which are based on the single-interaction-based stress and energy flux at the subatomic scale.

The time-averaged density-of-states and energy flux density distributions in the $\hat{\sigma}_{zz} - \hat{z}_s$ plane are presented, which are calculated by a single interaction between a solid atom and a liquid molecule for the overall interface [Fig. 22(a)]

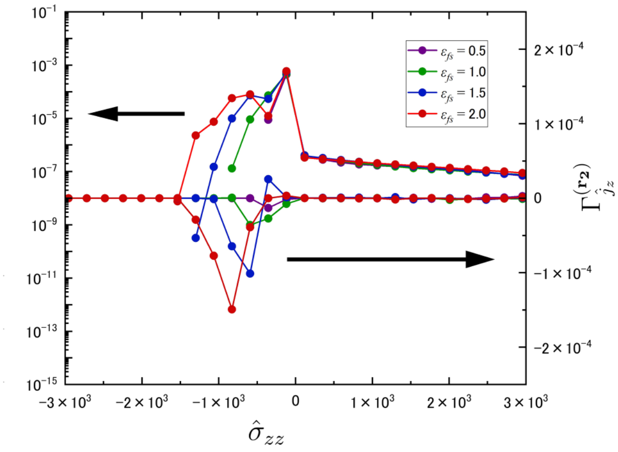

FIG. 21. Time-averaged density distribution $\Gamma^{(\mathbf{r}_2)}(\hat{\sigma}_{zz}) = \langle \int_{-\infty}^{\infty} \Gamma^{(\mathbf{r}_2,t)}(\hat{\sigma}_{zz}, \hat{v}_{z,+})\, d\hat{v}_{z,+} \rangle$ and energy flux density distribution $\Gamma^{(\mathbf{r}_2)}_{\hat{j}_z}(\hat{\sigma}_{zz}) = \langle \int_{-\infty}^{\infty} \hat{j}_z \Gamma^{(\mathbf{r}_2,t)}(\hat{\sigma}_{zz}, \hat{v}_{z,+})\, d\hat{v}_{z,+} \rangle$ for $\varepsilon_{fs} = 0.5,\ 1.0,\ 1.5,$ and 2.0. The values are obtained at $\mathbf{r_2} = (4.1, 3.5, 0.41)$.

at $\mathbf{r} = \mathbf{r}_1$ [Fig. 22(b)] and $\mathbf{r} = \mathbf{r}_2$ [Fig. 22(c)] for $\varepsilon_{fs} = 2.0$. The positions of $\mathbf{r}_1$ and $\mathbf{r}_2$ are shown in Figs. 18(a) and 20(a), respectively. The density-of-states distribution in Fig. 22(a) indicates that the solid-atom density is highest at $\hat{z}_s = -0.09$, which contains the first solid layer facing the liquid layer. Compared with the density-of-states distribution of the solid atoms in the first layer, the energy-flux distribution $\Gamma_{\hat{j}_z}$ in Fig. 22(a) can be interpreted as the occurrence of positive and negative energy transport when the solid atom in the contacting layer moves in positive (towards the liquid layer) and negative directions (away from the liquid layer), respectively, outside the stress band ($\hat{\sigma}_{zz} > 0$). Moreover, the positive and negative energy transports inside the band ($\hat{\sigma}_{zz} < 0$) correspond to the negative and positive directions of the solid-atom movement, respectively. The same property is detected at the subatomic scale [Fig. 22(b)]. Especially outside of the band, the distribution is not symmetric about $\hat{z}_s = -0.09$. Positive energy transport can occur in the higher single-interaction stress region, even when the solid atom moves against the liquid layer ($\hat{z}_s < -0.09$). The result at $\mathbf{r}_2$ [Fig. 22(c)], where a strong heat flux is not detected, exhibits a weak energy transfer outside the band, which suggests that the macroscopic energy transfer in Fig. 22(a) reflects the strong heat flux at the subatomic scale [Fig. 22(b)].

The thermal transport mechanism based on the 1D distributions along the positions of the solid atoms contributing to the local heat flux is detailed below. Figure 23 presents the time-averaged density distribution of the physical quantities in the z direction. Figure 23(a) shows the density of states $\Gamma(\hat{z}_s)$, energy flux $\Gamma_{\hat{j}_z}(\hat{z}_s)$, velocity of the liquid molecule $\Gamma_{\hat{v}_{z,l}}(\hat{z}_s)$, and sum of the velocities of the solid atom and liquid molecules $\Gamma_{\hat{v}_{z,+}}(\hat{z}_s)$. Figure 23(b) presents the density of states $\Gamma(\hat{z}_s)$, stress per single interaction $\Gamma_{\hat{\sigma}_{zz}}(\hat{z}_s)/\Gamma(\hat{z}_s)$, and sum of the velocities of the solid atom and liquid molecule per single interaction $\Gamma_{\hat{v}_{z,+}}(\hat{z}_s)/\Gamma(\hat{z}_s)$. Each result is presented for the regions inside and outside the stress band and for the entire

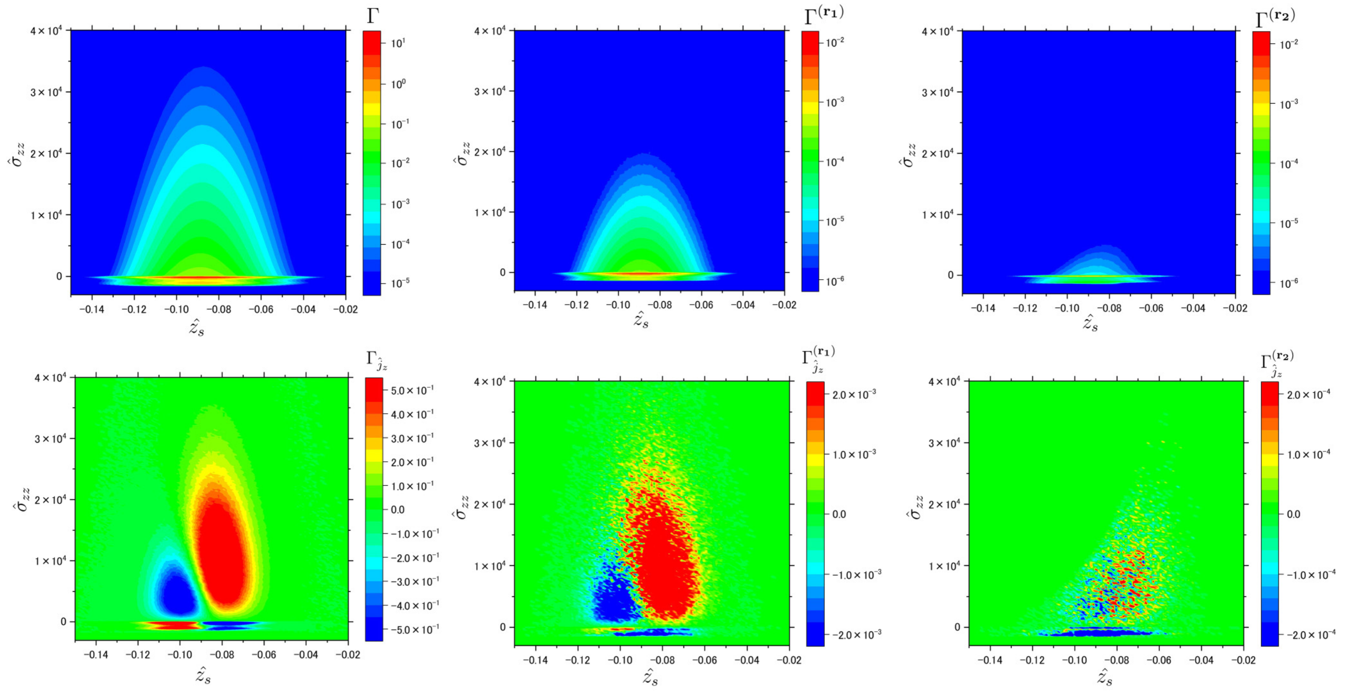

(a) Overall interface

(b) Local area at $\mathbf{r}_1$

(c) Local area at $\mathbf{r}_2$

FIG. 22. Time-averaged density-of-states and energy flux density distributions in the plane of the single-interaction-based stress $\hat{\sigma}_{zz}$ and position $\hat{z}_s$ for (a) the overall interface, (b) at $\mathbf{r} = \mathbf{r}_1$, and (c) at $\mathbf{r} = \mathbf{r}_2$, where each value is calculated within an area of $d\hat{\sigma}_{zz} \times d\hat{z}_s = 2.3 \times 10^2 \times 1.4 \times 10^{-3}$.

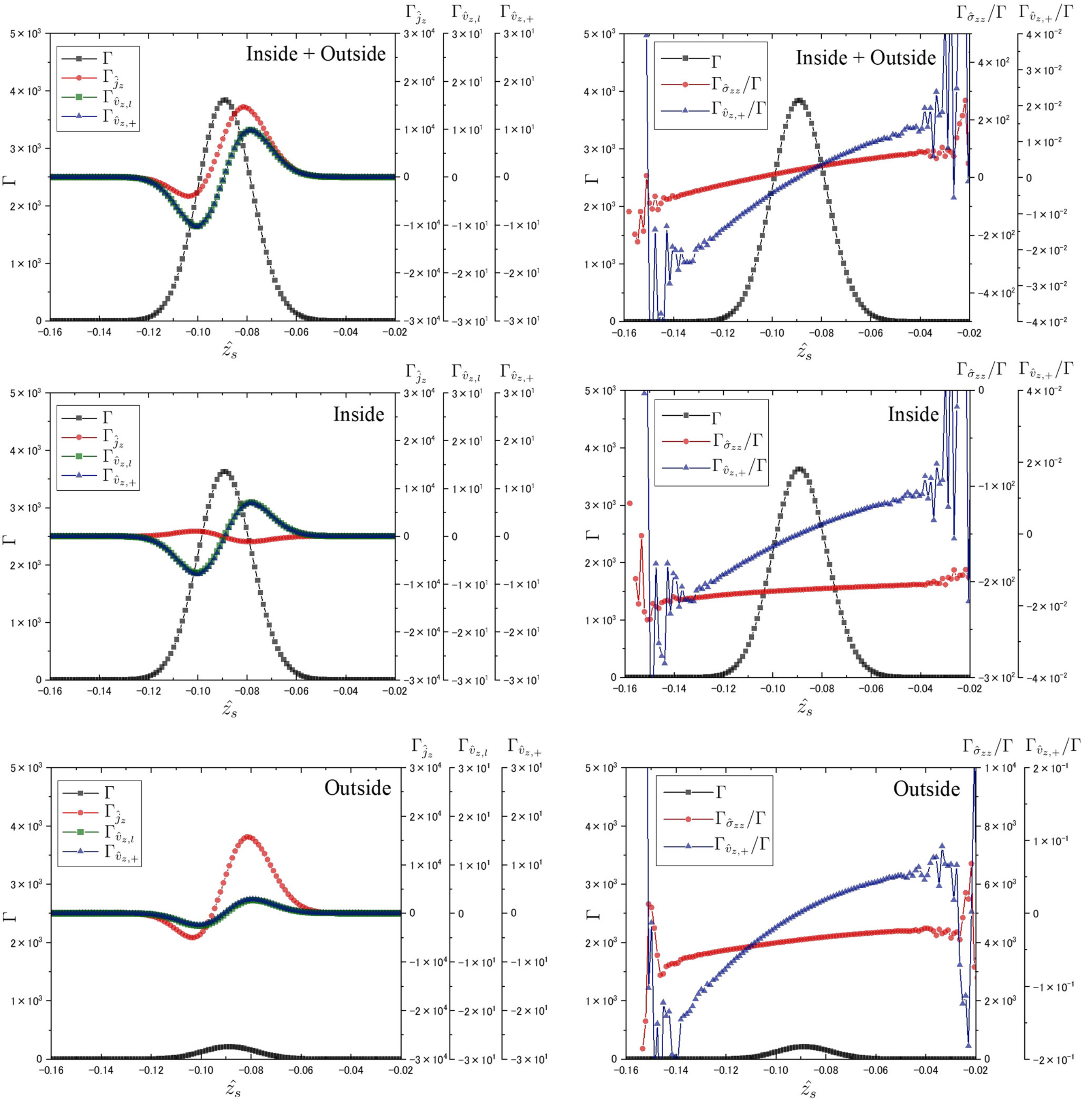

(a) (b)

FIG. 23. Time-averaged density distribution of the physical quantities in the z direction for the overall interface: (a) density of states $\Gamma(\hat{z}_s)$, energy flux $\Gamma_{\hat{j}_z}(\hat{z}_s)$, velocity of the liquid molecule $\Gamma_{\hat{v}_{z,l}}(\hat{z}_s)$, and sum of the velocities of the solid atom and liquid molecule $\Gamma_{\hat{v}_{z,+}}(\hat{z}_s)$; and (b) density of states $\Gamma(\hat{z}_s)$, stress per single interaction $\Gamma_{\hat{\sigma}_{zz}}(\hat{z}_s)/\Gamma(\hat{z}_s)$, and sum of the velocities of the solid atom and liquid molecule per single-interaction $\Gamma_{\hat{v}_{z,+}}(\hat{z}_s)/\Gamma(\hat{z}_s)$. The values for each case are obtained for the entire region (inside and outside), inside region, and outside region, of the stress band.

region (inside and outside the stress band). The density of states $\Gamma(\hat{z}_s)$ exhibits a peak at $\hat{z}_s = -0.09$, where the first solid layer exists as shown in Fig. 22. Calculating $\Gamma_{\hat{j}_z}(\hat{z}_s)$ outside the stress band reveals that positive and negative energy transports occur when the solid atom is near to and far from the liquid layer, respectively, from the most probable position. The amount of integration of the positive heat flux exceeds that of the negative heat flux, which implies that the sum of the positive and negative energy fluxes (net flux) is positive. The velocity distribution of the liquid $\Gamma_{\hat{v}_{z,l}}(\hat{z}_s)$ and distribution of the sum of the velocities of the solid atom and liquid molecule $\Gamma_{\hat{v}_{z,+}}(\hat{z}_s)$ are detected as highly similar

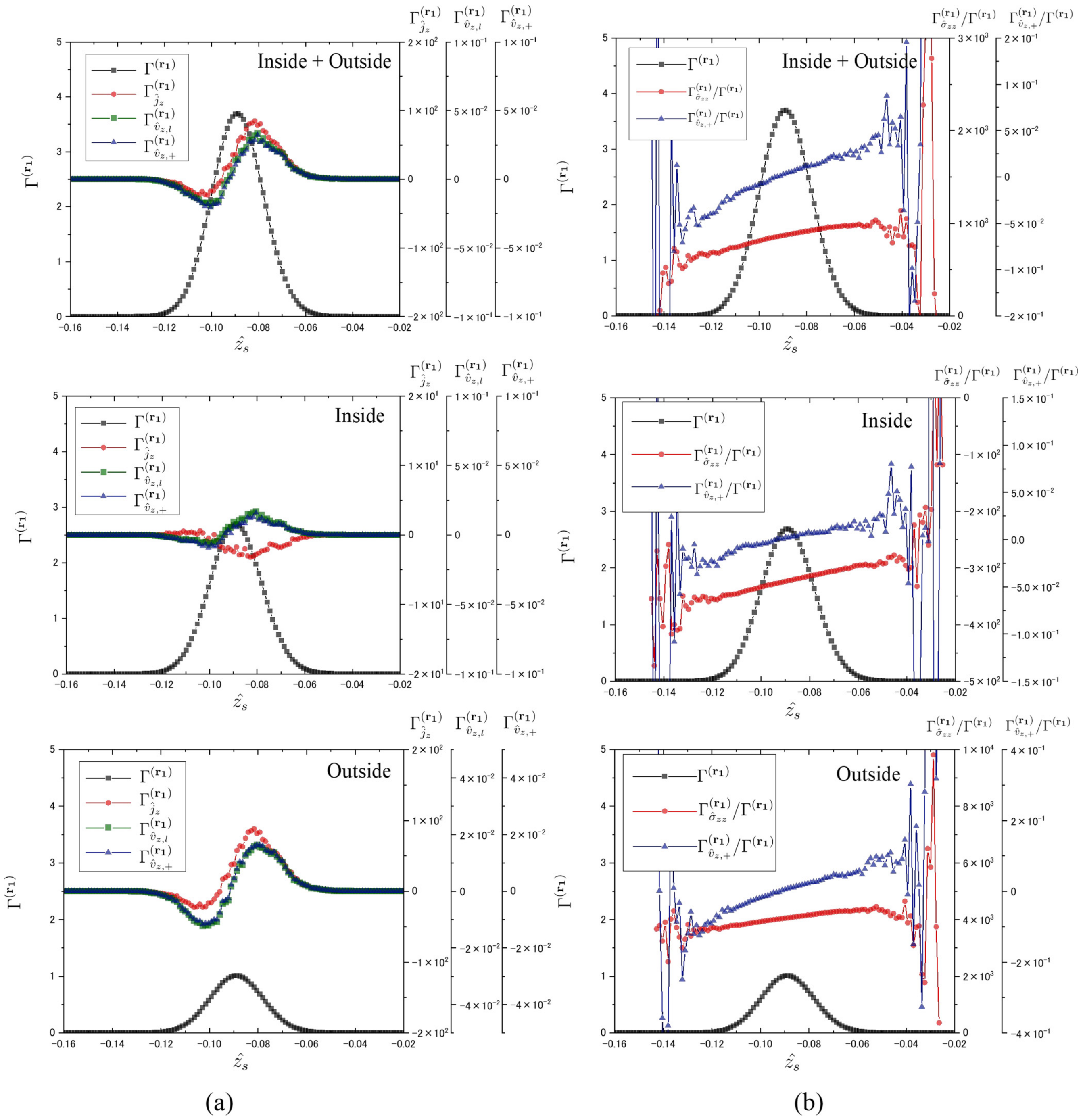

FIG. 24. Time-averaged density distribution of the physical quantities in the z direction at ($\mathbf{r} = \mathbf{r}_1$): (a) density of states $\Gamma^{(\mathbf{r}_1)}(\hat{z}_s)$, energy flux $\Gamma^{(\mathbf{r}_1)}_{\hat{j}_z}(\hat{z}_s)$, velocity of the liquid molecule $\Gamma^{(\mathbf{r}_1)}_{\hat{v}_{z,l}}(\hat{z}_s)$, and sum of the velocities of the solid atom and liquid molecule $\Gamma^{(\mathbf{r}_1)}_{\hat{v}_{z,+}}(\hat{z}_s)$; and (b) density of states $\Gamma^{(\mathbf{r}_1)}(\hat{z}_s)$, stress per single-interaction $\Gamma^{(\mathbf{r}_1)}_{\hat{\sigma}_{zz}}(\hat{z}_s)/\Gamma^{(\mathbf{r}_1)}(\hat{z}_s)$, and sum of the velocities of the solid atom and liquid molecule per single-interaction $\Gamma^{(\mathbf{r}_1)}_{\hat{v}_{z,+}}(\hat{z}_s)/\Gamma^{(\mathbf{r}_1)}(\hat{z}_s)$. The values for each case are obtained over the entire region (inside and outside), inside region, and outside region, of the stress band.

values, thus suggesting that the energy flux property is dependent on the liquid molecule velocity. Notably, the energy flux density distribution $\Gamma_{\hat{j}_z}(\hat{z}_s)$ inside the band exhibits an inverse trend to that outside the band; however, the influence is limited. These characteristics can be understood with reference to the results for the stress and liquid velocity per single interaction, as shown in Fig. 23(b). Outside the stress band, $\Gamma_{\hat{\sigma}_{zz}}(\hat{z}_s)/\Gamma(\hat{z}_s)$ exhibits a positive value with a positive gradient in the z direction, although $\Gamma_{\hat{v}_{z,+}}(\hat{z}_s)/\Gamma(\hat{z}_s)$ intersects the zero value at approximately $\hat{z}_s = -0.09$ with a positive gradient. The energy flux in Eq. (40) implies that this characteristic of $\Gamma_{\hat{\sigma}_{zz}}(\hat{z}_s)/\Gamma(\hat{z}_s)$ and $\Gamma_{\hat{v}_{z,+}}(\hat{z}_s)/\Gamma(\hat{z}_s)$ determines the

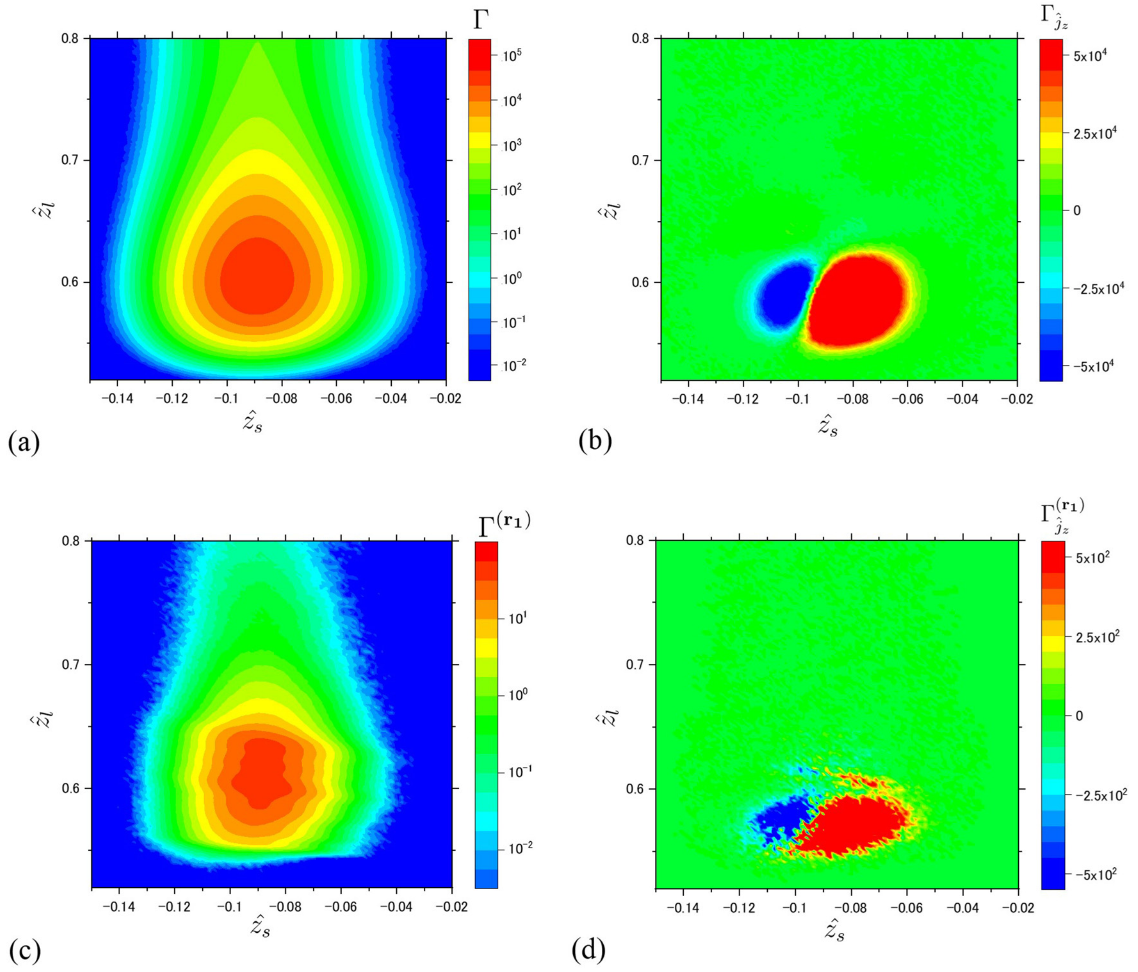

FIG. 25. Time-averaged density distribution and energy flux density distribution in the plane of the solid atom position $\hat{z}_s$ and the liquid molecule position $\hat{z}_l$ in the contacting solid-liquid layers in the case of $\varepsilon_{fs} = 2.0$ for the overall interface; (a) $\Gamma(\hat{z}_s, \hat{z}_l) = \langle \Gamma^{(t)}(\hat{z}_s, \hat{z}_l) \rangle$ and (b) $\Gamma_{\hat{j}_z}(\hat{z}_s, \hat{z}_l) = \langle \Gamma^{(t)}_{\hat{j}_z}(\hat{z}_s, \hat{z}_l) \rangle$. Similarly, for the subatomic scale ($\mathbf{r} = \mathbf{r}_1$): (c) $\Gamma^{(\mathbf{r}_1)}(\hat{z}_s, \hat{z}_l) = \langle \Gamma^{(\mathbf{r}_1,t)}(\hat{z}_s, \hat{z}_l) \rangle$ and (d) $\Gamma^{(\mathbf{r}_1)}_{\hat{j}_z}(\hat{z}_s, \hat{z}_l) = \langle \Gamma^{(\mathbf{r}_1,t)}_{\hat{j}_z}(\hat{z}_s, \hat{z}_l) \rangle$. The values are calculated within an area of $d\hat{\mathbf{z}}_l \times d\hat{\mathbf{z}}_s = 2.1 \times 10^{-3} \times 1.1 \times 10^{-3}$.

energy flux profile in Fig. 23(a). The inside region of the band, $\Gamma_{\hat{\sigma}_{zz}}(\hat{z}_s)/\Gamma(\hat{z}_s)$ exhibits a negative value in the z direction; thus, the energy flux inside the band exhibits an inverse result. As can be seen from Fig. 13, the contribution outside the band is dominant for the net energy flux, regardless of the low density of states. This is confirmed by the results shown in Fig. 23(a).

The results obtained at $\mathbf{r} = \mathbf{r_1}$ (Fig. 18) are presented in Figs. 24(a) and 24(b), which display the results at the subatomic scale. The macroscopic thermal transport is in accordance with the properties of the local transport quantities at the subatomic scale. In Sec. V we demonstrate that the heat flux is linearly proportional to the stress at a subatomic spatial resolution. From the results in Fig. 24, the characteristics of the local stress and its role in energy transfer are clarified when evaluated considering the solid-atom position. A high-stress field indicates that the stress acting on the solid atom is high, which allows for the solid atom to transfer energy and be influenced by large stress changes when moving in space. The large stress change generates a large difference between the positive and negative energy fluxes, which are dependent on the position of the solid atom in the temperature gradient direction.

Figure 25 reveals the influence of the positions of solid atoms and liquid molecules on the density-of-states and corresponding energy flux density distributions for the overall interface [Figs. 25(a) and 25(b)] and at $\mathbf{r} = \mathbf{r}_1$ [Figs. 25(c) and 25(d)]. In Fig. 25, $\hat{z}_s$ and $\hat{z}_l$ denote the z components of the solid atoms and liquid molecules, respectively. The results reveal that the thermal transport mechanism, as shown in Figs. 23 and 24, is not dependent on the liquid molecule positions. These influence only the range of positive and negative energy fluxes.

VIII. MECHANISM OF THERMAL TRANSPORT ACROSS SOLID-LIQUID INTERFACE BASED ON SINGLE-INTERACTION-BASED ENERGY FLUX: INFLUENCE OF TEMPERATURE GRADIENT

The influence of the temperature gradient in the system based on the single-interaction-based energy flux, which is

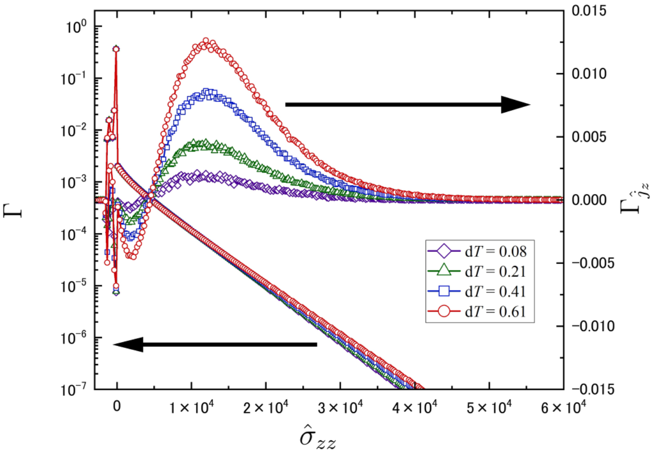

FIG. 26. Time-averaged density distribution $\Gamma(\hat{\sigma}_{zz})$ and energy flux density distribution $\Gamma_{\hat{j}_z}(\hat{\sigma}_{zz})$ in the single-interaction-based stress $\hat{\sigma}_{zz}$ for the temperature differences $\Delta T = 0.08, 0.21, 0.41$, and 0.61.

related to the origin of the thermal transport mechanism in the nonequilibrium state, is investigated in this section. Figure 26 presents the distribution functions of $\Gamma(\hat{\sigma}_{zz})$ and $\Gamma_{\hat{j}_z}(\hat{\sigma}_{zz})$ for the various temperature differences ($dT = 0.08$, 0.21, 0.41, and 0.61), where the result is obtained for the overall solid-liquid interface. Based on the results, almost the same profile as shown in Fig. 13 is confirmed, where positive and negative energy transport are detected outside the stress band ($\hat{\sigma}_{zz} > 0$), and the energy transport outside the band contributes dominantly to the net heat flux. The difference between the influences of the solid-liquid interaction strength (ε_{fs}) and the temperature gradient is reflected in the density-of-states distribution $\Gamma(\hat{\sigma}_{zz})$. The solid-liquid interaction strength influences the density change of the liquid molecules in the vicinity of the solid surface, which increases $\Gamma(\hat{\sigma}_{zz})$ outside the band for a higher interaction strength, as shown in Fig. 13. However, the change in $\Gamma(\hat{\sigma}_{zz})$ due to the temperature change in Fig. 26 is not evident, given that the density change is small, even under a large temperature gradient, in the nonequilibrium molecular dynamics simulation. This suggests that the energy transport per single interaction is enhanced by the influence of the velocity $\hat{v}_{z,+}$. With a decrease in the temperature gradient in the system, the energy transport outside the band decreases, which indicates a low thermal transport across the solid-liquid interface. Based on the results, it is concluded that the origin of the thermal transport across a solid-liquid interface with respect to the transport quantities at the subatomic scale is due to an imbalance between the energy transfer outside and inside the bands. This leads to a temperature gradient and net thermal transport across the interface, due to the high-stress field at the subatomic scale.

IX. CONCLUSION

In this study, the heat flux and stress at the subatomic scale are examined using the classical molecular dynamics method to clarify the origin of thermal transport across a solid-liquid interface. The system is modeled with the LJ potential, in which a temperature gradient is imposed, and a complete picture of the transport field is revealed at the solid-liquid interface. The heat flux and stress in the three dimensions are observed at a subatomic resolution between the contacting solid and liquid layers. The microscopic expression of the transport equations is extended to a form based on the density-of-states distributions defined in the variable space where the contributions of a single-particle movement and a single interaction between particles are considered. The transport quantities at the macroscopic and subatomic scales are related based on the density distributions with the single-interaction-based stress and energy flux, and the thermal transport mechanism at the solid-liquid interface is explained by an intrinsic transport property between a solid atom and liquid molecule at the interface. Furthermore, the influences of the solid-liquid interaction strength and the temperature gradient in the system are investigated to elucidate the properties of the field transport quantities at the subatomic scale and the origin of thermal transport across a solid-liquid interface. The conclusions can be summarized as follows.

The 3D structure of the heat flux detected at the subatomic scale exhibits directional qualities between the solid and liquid contacting layers due to the nonuniformity of the density of the solid atoms and liquid molecules at the interface. The evaluation of the influence of the interaction strength between solid atoms and liquid molecules reveals that the directional quality in the structure directly reflects the energy transport. With a decrease in the width of the heat-flux branch, a stronger heat flux is observed at the subatomic scale, which corresponds to the enhancement of the macroscopic thermal transport at a flat interface. The energy fluxes perpendicular to the macroscopic temperature gradient are observed at the subatomic scale, which are critical for more complex interfaces such as amorphous surfaces or functional interfaces with terminations. A correlation between the energy flux and stress at the subatomic scale is observed, in that the energy flux is positively and linearly correlated with the stress. Under macroscopic thermodynamic conditions, the ITC at the subatomic scale exhibits values reflecting the local heat flux, and the changes in the local ITC are mainly due to the stress changes in the corresponding subatomic space. Negative heat fluxes and stresses are observed at the subatomic scale, even when the macroscopic heat flux and pressure in the system are positive.

The density-of-states distribution based on the single-interaction-based stress and energy flux provides more detailed information than the microscopic expression of the transport equations. The transport quantities at the subatomic scale can be related to the macroscopic quantities based on the density distribution, in which the contributions of the single-interaction-based stress and energy flux to the local stress and energy flux at the subatomic spatial resolution play an important role in interpreting the local transport quantities. The density distribution in the plane of the single-interaction-based stress and other variables exhibits a bandlike behaviour (referred to as a “stress band” in this paper), where relatively high and low densities of states are detected inside and outside the stress band, respectively. The stress band reflects the intrinsic properties of the intermolecular force (van der Waals force in this study), i.e., the relatively short and long intermolecular distances corresponding to the states outside

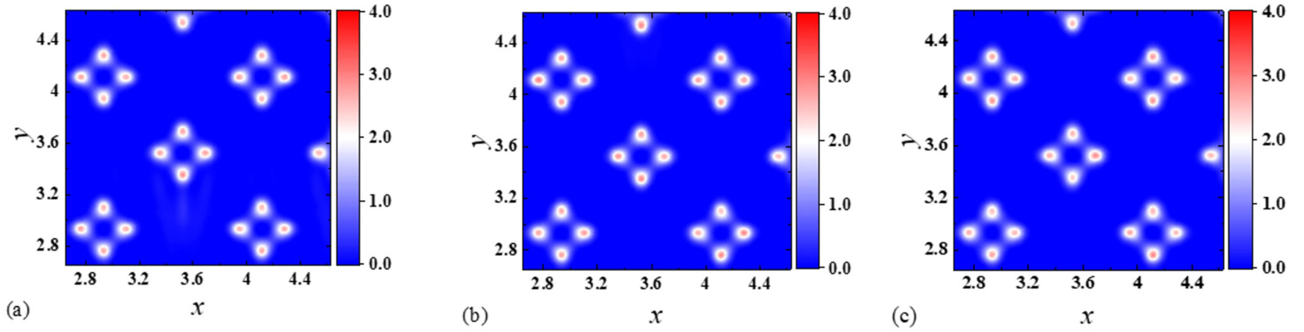

FIG. 27. Influence of the simulation box size in the *x*-*y* plane on the heat flux (*z* component) at the subatomic scale: (a) 8 lattices, (b) 12 lattices, and (c) 16 lattices. The values are calculated at $z = 0.18$ for $\varepsilon_{fs} = 2.0$. To obtain the time-averaged value, 5.0×10^9, 2.5×10^9, and 2.5×10^9 time steps are used in the cases of (a)–(c), respectively.

and inside the band, respectively. The net energy transport is composed of positive and negative energy transport inside and outside the band, where the net heat flux is dominated by the energy transport outside the band. In addition, the effect is more significant due to the high density of states for a strong solid-liquid interaction. The same property is observed at the subatomic scale with a focus on the strong directional energy flux in the 3D heat flux structure. When the effect inside the band is dominant, a negative heat flux and stress are observed at subatomic scales as time-averaged values.

The heat flux at the subatomic scale between the contacting solid and liquid layers is examined based on the energy transport property when the solid atom at the contacting layer is near to and far from the liquid phase, respectively, from the most probable position. Outside the stress band, positive and negative energy transports in the temperature gradient direction are observed when the solid atom at the contacting layer is near to and far from the liquid phase, respectively. Conversely, inside the band, an inverse trend is observed; however, the contribution to the net energy transport is not significant due to the low stress value. The positive and negative energy transports inside and outside the stress bands allow for a fundamental understanding of the thermal transport mechanism based on the field transport quantities. In the high-stress field at the subatomic scale, the energy transport rate is high, and the gradient of the stress with respect to the solid atom position at the contacting layer exhibits higher values, which allows for the solid atom to transfer more energy than that in the low-stress field.

The evaluation of the influence of the temperature gradient reveals the origin of the thermal transport across the solid-liquid interface with respect to the transport quantities at the subatomic scale. In particular, the energy transfer imbalance between the inside and outside the regions of the bands is found to induce the thermal transport mechanism at the solid-liquid interface, which is due to the nonuniformity of the stress field at the subatomic scale with a different energy transport rate. Commonly employed nonequilibrium molecular dynamics simulations impose large temperature gradients to evaluate the energy transport outside the band. Notably, actual thermal transport occurs under a significantly weak imbalance between the inside and outside the regions of the stress band.

With current computational resources, obtaining the 3D transport quantities requires a large computation time; thus, the representation of the fluctuation [35] is a more practical method for obtaining the related transport quantities. The visualization of the transport quantities at the subatomic scale provides valuable information for elucidating transport phenomena in an intuitive manner, such as computational fluid dynamics. Although the interpretation of the local transport quantities at the subatomic scale is described in this paper for the LJ (van der Waals force) potential, the stress band concept and the method of using the distribution function should be applicable to more complex systems, such as those that include Coulombic forces. Furthermore, the proposed method

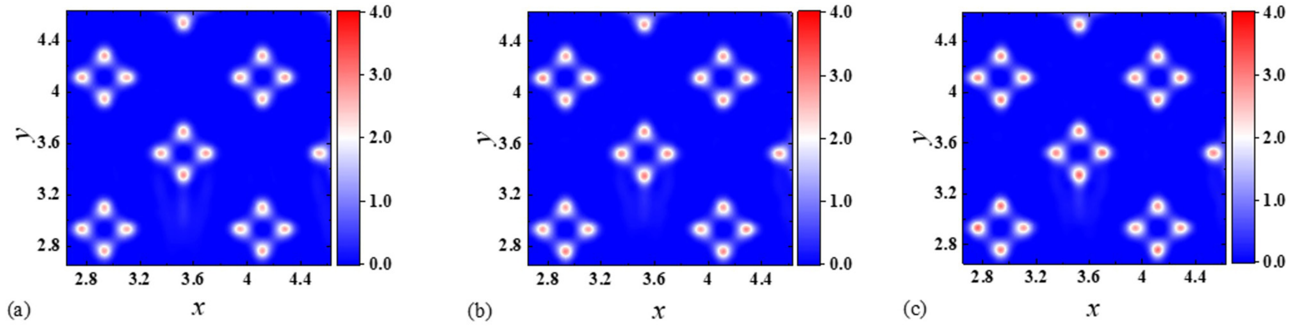

FIG. 28. Influence of the cutoff distance on the heat flux (*z* component) at the subatomic scale in the *x*-*y* plane: (a) 2.5, (b) 3.0, and (c) 3.5. The values are calculated at $z = 0.18$ for $\varepsilon_{fs} = 2.0$. To obtain the time-averaged value, 5.0×10^9, 2.5×10^9, and 2.5×10^9 time steps are used for the cases of (a)–(c), respectively.

is a promising approach for bulk materials at the atomic scale, in addition to various interfaces such as solid-solid, solid-gas, and liquid-gas interfaces. Selecting the appropriate variable in the distribution function is essential for the determination of the transport mechanism of atoms and molecules based on local transport quantities. Finally, the extension of this method to the phenomena that occur within a shorter time frame will be studied in the future.

ACKNOWLEDGMENT

This work was supported by JST, PRESTO Grant No. JPMJPR19I8 and JSPS KAKENHI Grant No. JP21K14096, Japan.

APPENDIX A: INFLUENCES OF SIMULATION CONDITIONS

The influence of the simulation conditions (i.e., model size and cutoff distance) on thermal transport across a solid-liquid interface is investigated. The adopted model is composed of eight lattices in the x and y directions. The heat flux (z component) in the eight-lattice model [Fig. 27(a)] is compared with those of 12- and 16-lattice models, as shown in Figs. 27(b) and 27(c), respectively, for $z = 0.18$ and $\varepsilon_{fs} = 2.0$. The results reveal that changes in the simulation box size have no significant influence on the local heat flux in the x-y plane.

As can be seen from Fig. 28, the z component of the heat flux at the subatomic scale is shown in the x-y plane for the cutoff distance of $r_c = 2.5$ [Fig. 28(a)], 3.0 [Fig. 28(b)], and 3.5 [Fig. 28(c)], where the values are obtained in the cases of $z = 0.18$ and $\varepsilon_{fs} = 2.0$. The results confirm that the cutoff distance does not influence the heat flux structure at the subatomic scale. The influence of the cutoff distance on the single-interaction-based energy flux is shown in Fig. 29. The values are obtained for the overall interface. For the overall stress region, changing the cutoff distance does not significantly influence the density of states and energy flux density. However, a slight influence is observed in the immediate vicinity of $\hat{\sigma}_{zz} = 0$ ($\hat{\sigma}_{zz}<0$). As an inherent property, a longer cutoff distance provides a higher density of states immediately below $\hat{\sigma}_{zz} = 0$ inside the stress band; however, there is a slight change in the corresponding heat flux due to the low-stress value.

APPENDIX B: SINGLE-INTERACTION-BASED ENERGY FLUX USING THE INNER PRODUCT OF SOLID-ATOM VELOCITY AND FORCE ACTING ON THE SOLID ATOM

For the heat flux calculation at the interface, we use Eq. (40), which considers the two types of particle velocities and provides more information than the inner product of the solid-atom velocity and force exerted on the solid atom, as mentioned previously. However, the heat flux at the subatomic scale, which is calculated using Eq. (24), is important. Figure 30 presents the result of $\Gamma_{\hat{j}_z}(\hat{\sigma}_{zz}, \hat{z}_s) = \langle \Gamma^{(t)}_{\hat{j}_z}(\hat{\sigma}_{zz}, \hat{z}_s)\rangle$ where $\hat{j}_z$ is calculated based on Eq. (24). As can be seen from the figure, the contribution to the net energy flux is dominant at $\hat{\sigma}_{zz} > 0$, and the positive and negative energy fluxes are not dependent on the solid atom position. Moreover, the negative

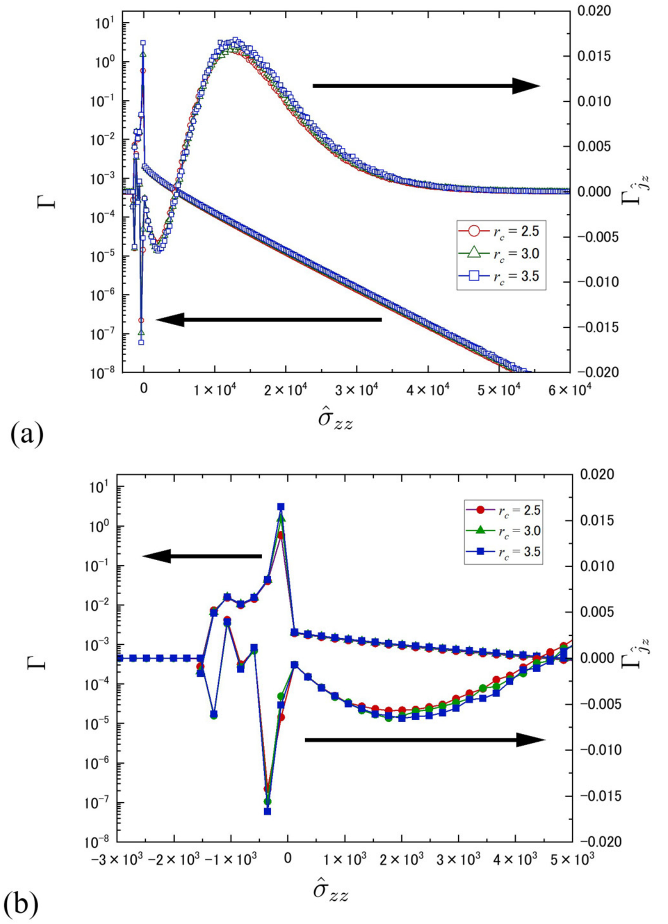

FIG. 29. (a) Influence of the cutoff distance on the single-interaction-based energy density in the cases of $r_c = 2.5$, 3.0, and 3.5 for $\varepsilon_{fs} = 2.0$. To obtain the time-averaged value, 5.0×10^9, 2.5×10^9, and 2.5×10^9 time steps are used for the cases of $r_c =$ 2.5, 3.0, and 3.5, respectively. (b) Enlarged view of the negative stress region.

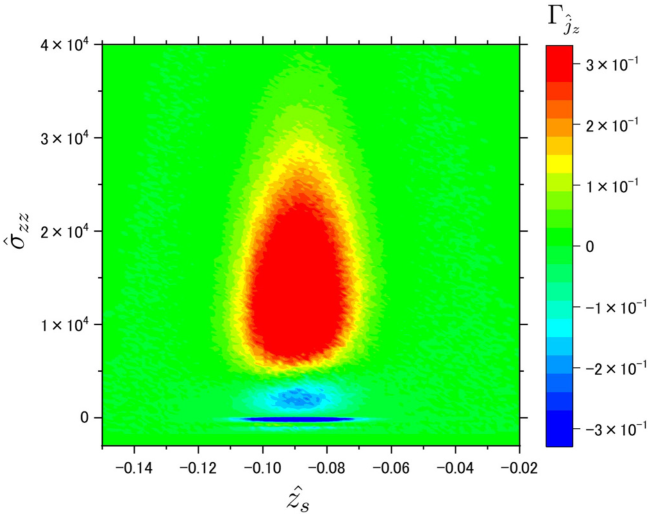

FIG. 30. Single-interaction-based energy flux distribution in the plane of the single-interaction stress and the z position of the solid atom; $\Gamma_{\hat{j}_z}(\hat{\sigma}_{zz}, \hat{z}_s)$, for the entire interface in the case of $\varepsilon_{fs} = 2.0$.

energy flux is dominant inside the band, because the field quantity does not contain complete information on the relative influence of the liquid molecule. The relative effects should therefore be considered using Eq. (40) to better understand the thermal transport across the interface based on the single-interaction-based energy flux.

[1] M. Kaviany, *Heat Transfer Physics* (Cambridge University Press, Cambridge, 2014).

[2] J. H. Irving and J. G. Kirkwood, J. Chem. Phys. **18**, 817 (1950).

[3] B. D. Todd, P. J. Daivis, and D. J. Evans, Phys. Rev. E **51**, 4362 (1995).

[4] K. Fujiwara and M. Shibahara, J. Chem. Phys. **141**, 034707 (2014).

[5] K. Fujiwara and M. Shibahara, J. Chem. Phys. **142**, 094702 (2015).

[6] M. P. Krafft and J. G. Riess, Chem. Rev. **109**, 1714 (2009).

[7] M. D. Losego, M. E. Grady, N. R. Sottos, D. G. Cahill, and P. V. Braun, Nat. Mater. **11**, 502 (2012).

[8] S. U. S. Choi and J. A. Eastman, ASME FED **231**, 99 (1995).

[9] P. Keblinski, J. A. Eastman, and D. G. Cahill, Mater. Today **8**, 36 (2005).

[10] S. Levin, J. Fritzsche, S. Nilsson, A. Runemark, B. Dhokale, H. Strom, H. Sunden, C. Langhammer, and F. Westerlund, Nat. Commun. **10**, 4426 (2019).

[11] M. E. Caplan, A. Giri, and P. E. Hopkins, J. Chem. Phys. **140**, 154701 (2014).

[12] L. Xue, P. Keblinski, S. R. Phillpot, S. U. S. Choi, and J. A. Eastman, Int. J. Heat Mass Transf. **47**, 4277 (2004).

[13] N. Shenogina, R. Godawat, P. Keblinski, and S. Garde, Phys. Rev. Lett. **102**, 156101 (2009).

[14] T. Ohara and D. Torii, J. Chem. Phys. **122**, 214717 (2005).

[15] D. Konatham and A. Striolo, Appl. Phys. Lett. **95**, 163105 (2009).

[16] M. Shibahara and T. Ohara, J. Therm. Sci. Technol. **6**, 247 (2011).

[17] Y. Ma, Z. Zhang, J. Chen, K. Sääskilahti, S. Volz, and J. Chen, Carbon **135**, 263 (2018).

[18] B.-Y. Cao, J.-H. Zou, G.-J. Hu, and G.-X. Cao, Appl. Phys. Lett. **112**, 041603 (2018).

[19] C. U. Gonzalez-Valle, S. Kumar, and B. Ramos-Alvarado, ACS Appl. Mater. Interf. **10**, 29179 (2018).

[20] K. M. Stocker and J. D. Gezelter, J. Phys. Chem. C **117**, 7605 (2013).

[21] Y. He and G. Galli, Phys. Rev. Lett. **108**, 215901 (2012).

[22] Z. Ge, D. G. Cahill, and P. V. Braun, Phys. Rev. Lett. **96**, 186101 (2006).

[23] T. Ohara, J. Chem. Phys. **111**, 9667 (1999).

[24] K. Saaskilahti, J. Oksanen, J. Tulkki, and S. Volz, Phys. Rev. E **93**, 052141 (2016).

[25] K. Fujiwara and M. Shibahara, Appl. Phys. Lett. **114**, 011601 (2019).

[26] K. Fujiwara and M. Shibahara, Sci. Rep. **9**, 13202 (2019).

[27] D. J. Evans and G. Morriss, *Statistical Mechanics of Nonequilibrium Liquids* (Cambridge University Press, Cambridge, 2008).

[28] B. D. Todd and P. J. Davis, *Nonequilibrium Molecular Dynamics: Theory, Algorithms and Applications* (Cambridge University Press, Cambridge, 2017).

[29] E. R. Smith, P. J. Daivis, and B. D. Todd, J. Chem. Phys. **150**, 064103 (2019).

[30] G. V. Paolini and G. Ciccotti, Phys. Rev. A **35**, 5156 (1987).

[31] S. B. Zhu and M. R. Philpott, J. Chem. Phys. **100**, 6961 (1994).

[32] B. Shi and V. K. Dhir, J. Chem. Phys. **130**, 034705 (2009).

[33] T. Ohara, J. Chem. Phys. **111**, 6492 (1999).

[34] T. Ohara and D. Suzuki, Micro. Thermophys. Eng. **4**, 189 (2000).

[35] K. Fujiwara and M. Shibahara, AIP Adv. **8**, 025124 (2018).